Anomalous rotational resonance spectra in magic-angle spinning NMR

Helmle, M.; Lee, Y.K.; Verdegem, P.J.E.; Feng, X.; Karlsson, T.; Lugtenburg, J.; ... ; Levitt, M.H.

Anomalous Rotational Resonance Spectra
in Magic-Angle Spinning NMR

M. Helmle,*,†,[1] Y. K. Lee,*,[2] P. J. E. Verdegem,†,[3] X. Feng,*,[4] T. Karlsson,*
J. Lugtenburg,† H. J. M. de Groot,† and M. H. Levitt*,[5]

*Physical Chemistry Division, Arrhenius Laboratory, Stockholm University, S-10691 Stockholm, Sweden; and †Leiden Institute of Chemistry,
Gorlaeus Laboratories, Leiden University, P.O. Box 9502, NL 2300 RA Leiden, The Netherlands

Magic-angle spinning NMR spectra of samples containing dilute spin-$\frac{1}{2}$ pairs display broadenings or splittings when a rotational resonance condition is satisfied, meaning that a small integer multiple of the spinning frequency matches the difference in the two isotropic shift frequencies. We show experimental rotational resonance NMR spectra of a $^{13}C_2$-labeled retinal which are in qualitative disagreement with existing theory. We propose an explanation of these anomalous rotational spectra involving residual heteronuclear couplings between the ^{13}C nuclei and the neighboring ^1H nuclei. These couplings strongly influence the rotational resonance ^{13}C spectrum, despite the presence of a strong radiofrequency decoupling field at the ^1H Larmor frequency. We model the residual heteronuclear couplings by differential transverse relaxation of the ^{13}C single-quantum coherences. We present a superoperator theory of the phenomenon and describe a numerical algorithm for rapid Liouville space simulations in periodic systems. Good agreement with experimental results is obtained by using a biexponential transverse relaxation model for each spin site. © 1999 Academic Press

Key Words: magic-angle spinning; rotational resonance; superoperators; COMPUTE; heteronuclear decoupling.

I. INTRODUCTION

Nuclear spin transitions may be driven by mechanical rotation of a solid sample. This process is particularly efficient at well-defined values of the sample rotation frequency ω_r, called the *rotational resonances* (RR) (*1–17*). The phenomenon has been investigated most thoroughly for the case of dilute pairs of spins-$\frac{1}{2}$ in nonequivalent molecular sites, in the presence of magic-angle spinning (MAS) (*18, 19*). Prominent rotational resonance phenomena are observed at the conditions $\omega_\Delta^{iso} = n\omega_r$, where the difference in isotropic chemical shift frequen-

cies is denoted ω_Δ^{iso}, and n is a small integer, called the rotational resonance order (*1–17*).

Rotational resonance has two main effects on the nuclear spin dynamics: (i) spectral broadenings and splittings and (ii) accelerated exchange of Zeeman magnetization between nearby molecular sites. Both effects may be used to estimate distances between nuclear spins, and hence, provide molecular structural information. Rotational resonance is widely used for this purpose in biological solid-state NMR (*10–17*).

Many applications of rotational resonance concern pairs of ^{13}C spins, introduced into organic molecules by specific isotopic labeling. The $^{13}C_2$-labeled molecules are often diluted in a matrix of unlabeled material, in order to isolate them from each other, on the timescale of the NMR experiment. In addition, a strong RF decoupling field is usually applied at the Larmor frequency of abundant spins, such as protons. Under these conditions, it is generally assumed that the ^{13}C pairs represent isolated 2-spin-$\frac{1}{2}$ systems, with simple and predictable spin dynamics.

The dynamics of the coupled spin pairs are readily simulated numerically (*20–23*). In many cases, all of the parameters in the spin Hamiltonian are known to a good approximation, including the chemical shift anisotropies and their orientations. This usually allows good agreement to be obtained between simulations and experimental results. For example, in a different paper (*8*), we present results on a $^{13}C_2$-labeled retinal sample at a rather low magnetic field of 4.702 T. The observed rotational resonance spectra are in good quantitative agreement with simulations for isolated 2-spin-$\frac{1}{2}$ pairs.

Surprisingly, this good agreement does *not* persist at higher magnetic fields. As shown below, the ^{13}C MAS NMR spectra of the same $^{13}C_2$-labeled retinal sample at a field of 9.402 T display strong and qualitative disagreement with the predictions of standard rotational resonance theory.

This is disconcerting. The agenda of using solid-state NMR for molecular structural studies would be at risk if the spectrum of a well-controlled model system were in serious discrepancy with theory.

In this paper, we propose that the RR spectral anomalies are caused by heteronuclear interactions between the $^{13}C_2$ pairs and

---

the abundant protons. In some cases, the model of isolated spin-$\frac{1}{2}$ pairs breaks down significantly, even in the presence of a strong proton decoupling field. This breakdown of the isolated spin-$\frac{1}{2}$ pair model is typically observed at high static fields and at high sample rotation frequencies. However, some samples display significant anomalies even under much milder conditions, as shown at the end of this paper.

It is important to realize that RR spectra are much more sensitive to decoupling imperfections than spectra taken off rotational resonance. When the rotational resonance condition is not satisfied, incomplete ^{1}H decoupling is associated with minor spectral perturbations, such as broad peak bases, which are easily overlooked. At rotational resonance, on the other hand, even minor decoupling imperfections may lead to strong perturbations of the entire ^{13}C NMR spectrum.

A full understanding of RR ^{13}C spectra is therefore intimately linked to the problem of heteronuclear decoupling in rotating solids—a complex subject in its own right (*24–32*). In the current paper, we employ two highly simplified representations of the heteronuclear decoupling problem, which are chosen because they allow a relatively simple treatment of the ^{13}C$_2$ spin dynamics.

In the *differential transverse relaxation* (DTR) model, the residual ^{1}H–^{13}C couplings are assumed to give rise to exponential transverse relaxation of the single-quantum ^{13}C coherences. The exponential decay constants are in general different for the two ^{13}C spin sites, reflecting the different local proton environments. As shown below, the *differential* in the transverse relaxation rates proves to be particularly significant. The DTR model provides a reasonable qualitative explanation of the observed ^{13}C spectra at rotational resonance. However, the DTR model fails to provide a consistent treatment of the ^{13}C spectra, both on and off RR.

The DTR model may be improved by taking into account the nonexponentiality of the transverse ^{13}C relaxation, which tends to become increasingly prominent as the static magnetic field and sample rotation frequency are increased. In the *multiple differential transverse relaxation* (MDTR) model, the nonexponential decay of the ^{13}C single-quantum coherences is modeled by superposing the results of two (or more) separate DTR calculations. The MDTR model has been chosen since it is the simplest model which allows the incorporation of nonexponential relaxation effects into the Liouville–von Neumann formalism. As will be shown, it is capable of good quantitative agreement between experiment and simulation, both on and off rotational resonance.

The rest of this paper is organized as follows. In Section II, we present experimental RR peakshape anomalies for the sample of ^{13}C$_2$-labeled retinal. In Section III, we present the theory of the RR peakshapes within the DTR and MDTR models. This includes a Liouville-space theory of single-quantum coherences at rotational resonance, which provides analytical expressions for the DTR peakshapes, under suitable approximations. We show that it is possible to attain consistent agreement
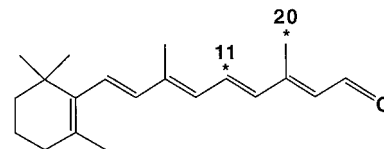
between experiment and numerical simulations within the framework of the MDTR model. In Section IV, we present alternative explanations for the observed RR peakshape anomalies and give our reasons for rejecting them. In Section V, we discuss the implications of these results for RR methodology and for solid-state NMR in general. In the Appendix, we describe a general COMPUTE algorithm for rapid Liouville-space simulations of powder-average spectra.

II. EXPERIMENTAL PEAKSHAPE ANOMALIES

Most of the experiments discussed in this paper concern the compound 11,20-^{13}C$_2$-all-*E*-retinal, which has the molecular structure and labeling scheme shown in Fig. 1. The distance between the C11 and C20 sites, as determined by X-ray diffraction (*33*), is 0.296 ± 0.001 nm.

The ^{13}C$_2$-labeled sample was prepared by known routes (*34*) from 99% ^{13}C-labeled starting materials. The labeled retinal was recrystallized from *n*-pentane at −20°C, together with nonlabeled all-*E*-retinal, in a molar ratio of 15:85. We refer to this diluted ^{13}C$_2$-labeled sample as **I**.

In a recent paper (*8*), we present ^{13}C rotational resonance spectra of **I** in a magnetic field of 4.702 T and show good agreement between experimental peakshapes and standard rotational resonance theory. Here, we examine the behavior of **I** at a higher magnetic field.

Figure 2a shows two regions of the NMR spectrum of **I** at a magnetic field of 9.402 T. The spectrum was taken at a spinning frequency of $\omega_r/2\pi = 12.192$ kHz, which satisfies the $n = 1$ RR condition. The decoupler field corresponded to a proton nutation frequency of 82 kHz. The spectrum shows two strong broad peaks from the ^{13}C labels, plus a number of smaller sharp peaks from naturally occurring ^{13}C spins in the rest of the molecule and the unlabeled matrix. The positions of these peaks coincide with those found in the spectrum of unlabeled all-*E*-retinal, obtained under identical conditions, which is shown in Fig. 2b.

A large number of isotopomers contribute to the spectrum in Fig. 2a. Apart from the deliberately introduced 11,20-^{13}C-isotopomer, there are numerous ^{13}C$_1$ and ^{13}C$_3$ isotopomers arising from the natural incidence of ^{13}C nuclei. It may be shown that the spectral contribution from the 11,20-^{13}C-isotopomer is isolated, to a very good approximation, by subtracting the natural abundance spectrum from the spectrum of **I**, multiplied by a suitable scaling factor, as shown in Fig. 2c. (Expanded views of the peaks are shown in Fig. 9d). To a good
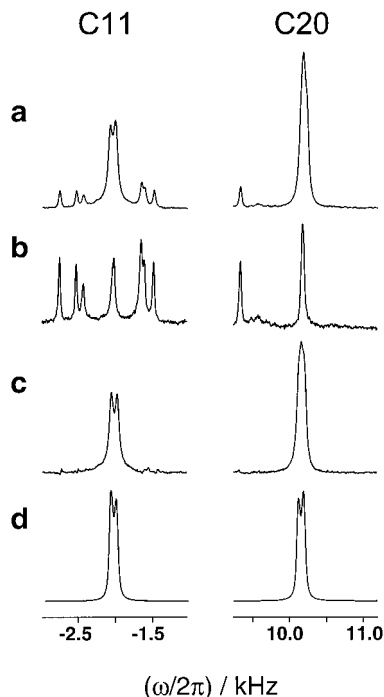

FIG. 1. Molecular structure and labeling scheme of 11,20-^{13}C$_2$-all-*E*-retinal. The ^{13}C spins are indicated by asterisks.

C11　　　C20

FIG. 2. ^{13}C spectra of all-E-retinal, at the $n = 1$ rotational resonance condition ($B_0 = 9.402$ T and $\omega_r/2\pi = 12.192$ kHz). Unmodulated proton decoupling was used. The decoupler field corresponded to a proton nutation frequency of 82 kHz. The spectral regions near the C11 and C20 centerbands are shown. (a) Spectrum of sample **I**. (b) Spectrum of unlabeled all-E-retinal. (c) Subtraction of (b) from (a), with weighting factors adjusted to minimize the visible natural abundance peaks. (d) Conventional simulation of (c), using transverse relaxation rate constants $r_{11} = r_{20} = 113$ s^{-1}. Other simulation parameters are given in Ref. (*69*). The experiments were performed on a BRUKER AMX-400 spectrometer using a 4-mm zirconia rotor.

approximation, this spectrum shows contributions from only the 11,20-^{13}C$_2$-isotopomer. The detailed arguments supporting the validity of this subtraction procedure are lengthy but straightforward and are not given here. One must take into account rotational resonance effects in some of the ^{13}C$_3$ isotopomers, as well as possible variations in the labeling levels of the C11 and C20 sites.

The spectrum of the 11,20-^{13}C$_2$-isotopomer may be simulated using the methods described in Ref. (*5*). The result is shown in Fig. 2d. This simulation employed Lorentzian peak broadening, corresponding to a peakwidth of 36.0 Hz (this corresponds to the width at half height of the C20 peak, measured at a spinning frequency of 10.000 kHz, i.e., well off rotational resonance). The simulated spectrum is in serious disagreement with the experimental spectrum shown in Fig. 2c. The most glaring discrepancy is found for the most shielded peak, attributed to the C20 site. The simulation predicts a clean splitting of this peak, while the experiment reveals no such splitting, only a tent-like structure.

The simulation of the C11 peak is in closer agreement with the experimental result. However, even here, there are some discrepancies. The experimental C11 peak has a broader base

than the simulated peak. The dip in the center of the C11 peak is slightly deeper than that predicted by the simulation. These minor discrepancies prove to be significant.

The spectrum of **I** appears to be quite normal when the spinning frequency is not close to a rotational resonance. Figure 3a shows the ^{13}C spectrum at a spinning frequency of $\omega_r/2\pi = 10.000$ kHz, with the same decoupler field as in Fig. 2a. After subtraction of the natural abundance background (Fig. 3b), the spectral peaks of both labeled sites are rather narrow, as shown in Fig. 3c. The peak widths at half maximum are 40.1 Hz for the C11 site and 36.0 Hz for the C20 site. Although the general form of the peaks is unremarkable, the C11 peak does have a slightly broad base. Expanded views of the peaks are shown in Fig. 10d.

Verdegem and co-workers (*13*) studied anomalous RR spectra for a series of labeled retinals, at a field of 9.402 T. In all cases, they found spectra of a similar form, with the less-shielded peak split and the more-shielded peak unsplit. They analyzed the splittings of the less-shielded peak and showed that there was a good empirical relationship between the splittings and the dipole–dipole couplings, as calculated from the X-ray structure. The split C11 peak could be described qualitatively using standard RR simulations assuming isolated ^{13}C$_2$ spin pairs. However, it was not possible to explain the anomalous form of the more-shielded peaks.

C11　　　C20
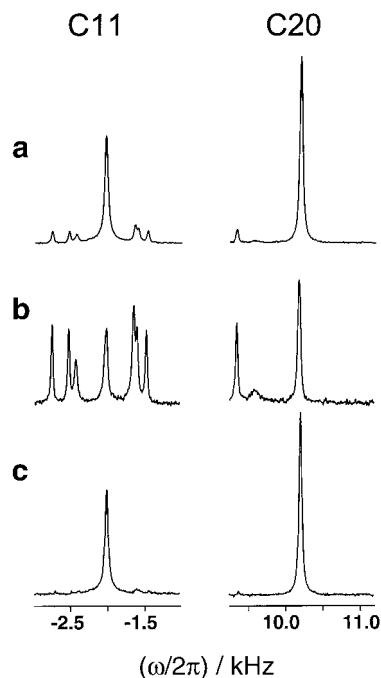

FIG. 3. ^{13}C spectra of all-E-retinal at 9.402 T, well off the $n = 1$ rotational resonance condition ($\omega_r/2\pi = 10.000$ kHz). The decoupler conditions were identical to those in Fig. 2. (a) Spectrum of sample **I**. (b) Spectrum of unlabeled all-E-retinal. (c) Subtraction of (b) from (a), with weighting factors adjusted to minimize the visible natural abundance peaks.

III. PEAKSHAPE THEORY

Spin Interactions

Spin Hamiltonian. Details of the spin-pair Hamiltonian in a rotating solid were given before (5). The basic equations are repeated here to correct some sign errors and to take into account the sense of the Larmor frequency (35).

The high-field Hamiltonian for two homonuclear spins-$\frac{1}{2}$ in nonequivalent molecular sites j and k may be written

$$\mathcal{H} = \mathcal{H}_j + \mathcal{H}_k + \mathcal{H}_{jk}, \qquad [1]$$

where $\mathcal{H}_j$ and $\mathcal{H}_k$ represent the one-spin interactions, and $\mathcal{H}_{jk}$ represents the interaction between the spins. These interactions are

$$\mathcal{H}_j = \omega_j S_{jz}$$

$$\mathcal{H}_k = \omega_k S_{kz}$$

$$\mathcal{H}_{jk} = \mathcal{H}_A + \mathcal{H}_B, \qquad [2]$$

with the two spin–spin interaction terms

$$\mathcal{H}_A = \omega_A 2 S_{jz} S_{kz}$$

$$\mathcal{H}_B = \omega_B \tfrac{1}{2} \{ S_j^+ S_k^- + S_j^- S_k^+ \}. \qquad [3]$$

The Larmor frequencies of the spins in sites j and k are denoted by ω_j and ω_k. The spin–spin coupling is denoted by two terms ω_A and ω_B, which are specified below.

Reference frames. Define a three-dimensional reference frame M which is fixed with respect to the molecule, another reference frame R which is fixed with respect to the rotor, and a further reference frame L which is fixed with respect to the external magnetic field. The z-axis of frame M is defined to be parallel with the vector joining the molecular sites j and k, the z-axis of frame R is defined to be parallel to the rotor axis, and the z-axis of frame L is defined to be parallel to the static magnetic field. The relative orientation of two reference frames, for example M and R, may be specified by an Euler angle triplet $\Omega_{MR} = \{ \alpha_{MR}, \beta_{MR}, \gamma_{MR} \}$, defined according to the convention in Ref. (36).

A powder sample contains a large number of molecules with a uniform distribution of orientations Ω_{MR}. The observed NMR signal is an average of signals over all possible values of the three Euler angles α_{MR}, β_{MR}, and γ_{MR}.

For a sample rotating at constant angular frequency ω_r about an axis subtending an angle β_{RL} with the external magnetic field, the Euler angle α_{RL} is given by

$$\alpha_{RL} = \alpha_{RL}^0 - \omega_r t, \qquad [4]$$

where the angle α_{RL}^0 describes the relative orientation of the

frames R and L at the time origin $t = 0$, defined as the start of NMR signal acquisition. In nonsynchronized experiments, the angle α_{RL}^0 takes random values from transient to transient. The negative sign in Eq. [4] is consistent with the Euler angle convention mentioned above. In the case of exact magic-angle spinning the angle β_{RL} is equal to arctan $\sqrt{2}$.

Chemical shift interactions. The chemical shift tensor of a site j is defined by the three principal values δ_{xx}^j, δ_{yy}^j, and δ_{zz}^j, and the Euler angles $\Omega_{PM}^j = \{ \alpha_{PM}^j, \beta_{PM}^j, \gamma_{PM}^j \}$ specifying the relative orientation of the CSA principal axis frame P_j and the molecular frame. The symbol δ refers consistently to *deshielding*. By convention, the principal values (and hence the principal axes) are assigned through $|\delta_{zz}^j - \delta_j^{iso}| > |\delta_{xx}^j - \delta_j^{iso}| \geq |\delta_{yy}^j - \delta_j^{iso}|$, where the isotropic chemical shift is $\delta_j^{iso} = \frac{1}{3} \{ \delta_{xx}^j + \delta_{yy}^j + \delta_{zz}^j \}$. The chemical shift anisotropy δ_j^{aniso} and asymmetry parameter η_j are defined through $\delta_j^{aniso} = \delta_{zz}^j - \delta_j^{iso}$ and $\eta_j = (\delta_{yy}^j - \delta_{xx}^j)/\delta_j^{aniso}$.

For site j, the isotropic chemical shift frequency in the rotating reference frame is defined through

$$\omega_j^{iso} = \omega_0 \delta_j^{iso} - \omega_{ref}, \qquad [5]$$

where ω_{ref} is the signed spectrometer reference frequency, given by

$$\omega_{ref} = -(\text{sign } \gamma) \omega_{carrier}, \qquad [6]$$

and $\omega_{carrier}$ is the (positive) angular frequency of the RF carrier wave (35). The Larmor frequency of the nuclear spins in the field B_0 is given by $\omega_0 = -\gamma B_0$, where γ is the magnetogyric ratio (35).

The periodically modulated Larmor frequencies ω_j and ω_k are conveniently written as Fourier series, for example,

$$\omega_j = \sum_{m=-2}^{+2} \omega_j^{(m)} \exp\{ im \omega_r t \}, \qquad [7]$$

with the Fourier coefficients

$$\omega_j^{(m)} = \omega_j^{iso} \delta_{m0} + [A_j^{aniso}]_m^R \exp\{ -im \alpha_{RL}^0 \} d_{m0}^2(\beta_{RL}). \qquad [8]$$

The chemical shift anisotropy tensor of site j is transformed from the principal axis frame to the rotor-fixed frame through successive $P_j \rightarrow M \rightarrow R$ transformations according to

$$[A_j^{aniso}]_m^R = \sum_{m'', m'} [A_j^{aniso}]_{m''}^P D_{m''m'}^2(\Omega_{PM}^j) D_{m'm}^2(\Omega_{MR}). \qquad [9]$$

The components of the CSA tensor of site j, in its own principal axis frame, are given in frequency units by

$$[A_j^{\mathrm{aniso}}]_{-2}^P = [A_j^{\mathrm{aniso}}]_{+2}^P = -6^{-1/2}\eta_j\delta_j^{\mathrm{aniso}}\omega_0$$

$$[A_j^{\mathrm{aniso}}]_{-1}^P = [A_j^{\mathrm{aniso}}]_{+1}^P = 0$$

$$[A_j^{\mathrm{aniso}}]_0^P = \delta_j^{\mathrm{aniso}}\omega_0. \qquad [10]$$

Similar equations apply for site k.

Spin–spin interactions. The two components of the spin–spin coupling are periodic and may be written as Fourier series:

$$\omega_A = \sum_{m=-2}^{+2} \omega_A^{(m)}\exp\{im\omega_r t\}$$

$$\omega_B = \sum_{m=-2}^{+2} \omega_B^{(m)}\exp\{im\omega_r t\}, \qquad [11]$$

$$\mathcal{H} = \tfrac{1}{2}\begin{pmatrix} \omega_j + \omega_k + \omega_A & & & \\ & \omega_j - \omega_k + \omega_A & \omega_B & \\ & \omega_B & -\omega_j + \omega_k - \omega_A & \\ & & & -\omega_j - \omega_k + \omega_A \end{pmatrix}. \qquad [17]$$

where the Fourier coefficients are given by

$$\omega_A^{(m)} = \pi J_{jk}\delta_{m0} + [A_{jk}^{\mathrm{aniso}}]_m^R\exp\{-im\alpha_{RL}^0\}d_{m0}^2(\beta_{RL})$$

$$\omega_B^{(m)} = 2\pi J_{jk}\delta_{m0} - [A_{jk}^{\mathrm{aniso}}]_m^R\exp\{-im\alpha_{RL}^0\}d_{m0}^2(\beta_{RL}). \qquad [12]$$

Here J_{jk} is the isotropic part of the indirect dipole–dipole coupling (J-coupling), and $[A_{jk}^{\mathrm{aniso}}]_m^R$ are the components of the spin–spin coupling anisotropy in the rotor-fixed frame. If the anisotropic J-coupling and molecular motion are negligible, the rotor-frame components are given by

$$[A_{jk}^{\mathrm{aniso}}]_m^R = b_{jk}D_{0m}^2(\Omega_{MR}), \qquad [13]$$

where the through-space spin–spin coupling constant is equal to

$$b_{jk} = -\frac{\mu_0}{4\pi}\frac{\gamma^2\hbar}{r_{jk}^3} \qquad [14]$$

and r_{jk} is the internuclear distance.

Hilbert space basis. It is convenient to choose an orthonormal basis spanned by the following spin-pair state functions:

$$|1\rangle = |+\tfrac{1}{2}, +\tfrac{1}{2}\rangle$$

$$|2\rangle = |+\tfrac{1}{2}, -\tfrac{1}{2}\rangle$$

$$|3\rangle = |-\tfrac{1}{2}, +\tfrac{1}{2}\rangle$$

$$|4\rangle = |-\tfrac{1}{2}, -\tfrac{1}{2}\rangle \qquad [15]$$

These state functions are simultaneous eigenfunctions of the individual z-angular momenta of the two spins:

$$S_{jz}|m_j, m_k\rangle = m_j|m_j, m_k\rangle$$

$$S_{kz}|m_j, m_k\rangle = m_k|m_j, m_k\rangle. \qquad [16]$$

The spin-pair Hamiltonian may be expressed in this basis as a 4×4 matrix:

Superoperator Theory

In order to explain the anomalous RR peakshapes, it is necessary to extend the model of isolated spin-$\tfrac{1}{2}$ pairs. There are many possible ways to do this. For example, one could include some additional spins, such as the nearest proton neighbors, in the theoretical treatment. However, rigorous calculations of this kind are problematic, since the real sample contains an essentially infinite network of coupled protons, while accurate numerical calculations rapidly become intractable for more than a few additional spins. In this article, we take into account the residual couplings to the proton network by including dissipative terms in the spin dynamics. This provides a reasonable phenomenological model of the experimental behavior, while retaining the essential simplicity of the 2-spin-$\tfrac{1}{2}$ system.

The simplest model of imperfect proton decoupling is called the *differential transverse relaxation model.* The residual contact of the ^{13}C with the ^{1}H spins is parameterized by two rate constants for exponential relaxation, denoted r_j and r_k. These rate constants are the inverses of the corresponding transverse relaxation time constants T_2. The different proton environments of the coupled ^{13}C spins are emulated by allowing these rate constants to be unequal. One expects that the rate constants for ^{13}C spins in different types of molecular sites conform to

the rough scheme quaternary < methyl < methene < methylene. The high rate constant for methylene carbons conforms to the empirical observation that ^{13}C spins in such sites are "hard to decouple"—presumably because each ^{13}C has a large through-space coupling to two protons, which have a large through-space coupling with each other. The low rate constant for methyl ^{13}C spins is associated with the generally rapid thermal jump motion around the local threefold axis, which reduces the effective heteronuclear and homonuclear couplings.

The DTR rate constants may also include other sources of transverse relaxation, such as modulation of the ^{13}C spin interactions by molecular motion. However, additional relaxation mechanisms are expected to be unimportant in the experimental system studied here.

The DTR model has the advantage of simplicity. The dynamics of the ^{13}C spin pairs may be treated using a superoperator formalism, without *explicit* consideration of the proton spins. Nevertheless, it should be stressed that, at some point, it is necessary to discuss how the two relaxation rate constants r_j and r_k depend on the heteronuclear dipolar couplings, the proton decoupler field, the sample rotation frequency, and the static magnetic field. We return to this point below.

Liouvillian. The simultaneous influence of coherent and incoherent interactions may be treated using the Liouville–von Neumann equation,

$$\frac{d}{dt}\rho = -i[\mathcal{H}, \rho] + \hat{\Gamma}\rho, \qquad [18]$$

where the spin density operator for a given molecular orientation is denoted ρ and $\hat{\Gamma}$ is the relaxation superoperator, including thermal polarization terms (37–39). This equation is valid if the fluctuating interactions are sufficiently small compared to the inverse of their own correlation times (the "Redfield limit" (40)).

In the present context, the Redfield conditions are satisfied if the local fields produced by the proton spins fluctuate very rapidly. These rapid local field fluctuations are generated by the proton decoupler field, which rapidly rotates the proton spin polarizations and the strong interactions of the protons with each other. The use of the Liouville–von Neumann equation implies that the decay of the ^{13}C transverse magnetization components is exponential, or equivalently, that the ^{13}C spectral peakshapes are Lorentzian, in the absence of rotational resonance effects.

The evolution of the spin density operator in the presence of Redfield-regime relaxation may be analyzed using superoperators (37). Define a set of basis operators Q_u which are orthonormal in the sense

$$\mathrm{Tr}\{Q_u^\dagger Q_v\} = \delta_{uv}. \qquad [19]$$

The following definitions establish the Liouville operator space:

$$|Q_u) = Q_u$$
$$(Q_u| = Q_u^\dagger$$
$$(Q_u|Q_v) = \mathrm{Tr}\{Q_u^\dagger Q_v\}. \qquad [20]$$

The Liouville–von Neumann equation may be rewritten as a first-order, homogeneous, differential equation,

$$\frac{d}{dt}|\rho) = \hat{L}|\rho), \qquad [21]$$

where the generator of the superoperator evolution ("Liouvillian") is given by

$$\hat{L} = -i\hat{\mathcal{H}}^{\mathrm{comm}} + \hat{\Gamma}, \qquad [22]$$

and $\hat{\mathcal{H}}^{\mathrm{comm}}$ is the Hamiltonian commutation superoperator, defined as

$$\hat{\mathcal{H}}^{\mathrm{comm}}|Q_u) = |[\mathcal{H}, Q_u]). \qquad [23]$$

Operator basis. A suitable basis for Liouville space is provided by the set of all shift and projection operators generated by pairs of states $\{|1\rangle \ldots |4\rangle\}$:

$$C_{rs} = |r\rangle\langle s|. \qquad [24]$$

It is easily verified that this 16-dimensional operator basis is orthonormal. We will call these operators "coherence operators" and the basis the "coherence basis." "Population operators" such as $|1\rangle\langle 1|$ are included in this basis.

The coherence operators are eigenoperators under commutation with the total z-angular momentum S_z,

$$\hat{S}_z^{\mathrm{comm}}|C_{rs}) = |[S_z, C_{rs}]) = p_{rs}|C_{rs}), \qquad [25]$$

where the eigenvalue p_{rs} is called the coherence order (41, 42). The relevant coherence orders are

$$p_{14} = +2$$
$$p_{24} = p_{34} = p_{12} = p_{13} = +1$$
$$p_{11} = p_{22} = p_{33} = p_{44} = p_{23} = p_{32} = 0$$
$$p_{42} = p_{43} = p_{21} = p_{31} = -1$$
$$p_{41} = -2. \qquad [26]$$

Hamiltonian commutation superoperator. In the absence of applied RF fields, the high-field truncated Hamiltonian commutes with the total z-angular momentum operator,

$$\hat{S}_z^{\text{comm}} | \mathcal{H}) = 0. \qquad [27]$$

As shown in the Appendix to Ref. (7), this property enforces the selection rule

$$(C_{rs} | \hat{\mathcal{H}}^{\text{comm}} | C_{uv}) = 0 \quad \text{if } p_{rs} \neq p_{uv}. \qquad [28]$$

This implies that the Hamiltonian commutation superoperator is block-diagonal in the coherence basis:

$$\hat{\mathcal{H}}^{\text{comm}} = \begin{pmatrix} \hat{\mathcal{H}}_{+2}^{\text{comm}} & & & & \\ & \hat{\mathcal{H}}_{+1}^{\text{comm}} & & & \\ & & \hat{\mathcal{H}}_{0}^{\text{comm}} & & \\ & & & \hat{\mathcal{H}}_{-1}^{\text{comm}} & \\ & & & & \hat{\mathcal{H}}_{-2}^{\text{comm}} \end{pmatrix}, \qquad [29]$$

where the block $\hat{\mathcal{H}}_{+2}^{\text{comm}}$ has dimension 1×1, the block $\hat{\mathcal{H}}_{+1}^{\text{comm}}$ has dimension 4×4, the block $\hat{\mathcal{H}}_{0}^{\text{comm}}$ has dimension 6×6, and so on.

Coherences of order -1 are observable by quadrature detection (35). Since this article only concerns the directly observed NMR spectrum, our attention may be restricted to the block $\hat{\mathcal{H}}_{-1}^{\text{comm}}$. The behavior of the zero-quantum block has been studied in detail elsewhere (7).

The matrix representation of the Hamiltonian commutation superoperator is readily calculated using the property

$$(C_{ab} | \hat{\mathcal{H}}^{\text{comm}} | C_{cd}) = \text{Tr}\{|b\rangle\langle a| [\mathcal{H}, |c\rangle\langle d|]\}$$
$$= \mathcal{H}_{ac}\delta_{bd} - \mathcal{H}_{db}\delta_{ac}. \qquad [30]$$

Since the Hamiltonian operator $\mathcal{H}$ is block-diagonal in the basis of Eq. [15], the 4×4 block $\hat{\mathcal{H}}_{-1}^{\text{comm}}$ is block-diagonal in the coherence basis. The two 2×2 blocks are denoted $\hat{\mathcal{H}}_a^{\text{comm}}$ and $\hat{\mathcal{H}}_b^{\text{comm}}$:

$$\hat{\mathcal{H}}_{-1}^{\text{comm}} = \begin{pmatrix} \hat{\mathcal{H}}_a^{\text{comm}} & 0 \\ 0 & \hat{\mathcal{H}}_b^{\text{comm}} \end{pmatrix}. \qquad [31]$$

The basis operators for the $\hat{\mathcal{H}}_a^{\text{comm}}$ block are $\{|C_{21}), |C_{31})\}$, while the basis operators for the $\hat{\mathcal{H}}_b^{\text{comm}}$ block are $\{|C_{43}), |C_{42})\}$.

This block-diagonalization has a clear physical interpretation: Since no RF fields are applied, and the spinning frequency is small compared to the Larmor frequency, the sample rotation only drives transitions between states with very similar energies, and hence with the same value for the total spin angular
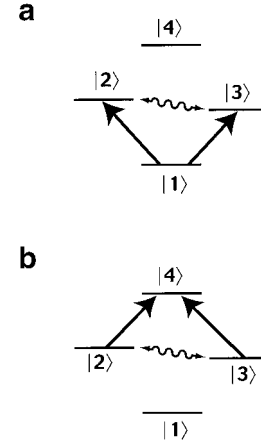

FIG. 4. Coherence transfer processes in the 2-spin-$\frac{1}{2}$ system. The rotational motion drives transitions between states $|2\rangle$ and $|3\rangle$, leading to transfer of amplitude between coherences $|C_{21})$ and $|C_{31})$ (block a) and between coherences $|C_{42})$ and $|C_{43})$ (block b).

momentum along the field. For a spin-$\frac{1}{2}$ pair, only the two central eigenstates $|2\rangle$ and $|3\rangle$ participate in the rotor-driven spin dynamics. It follows that the coherence $C_{21} = |2\rangle\langle 1|$ may be converted into a coherence $C_{31} = |3\rangle\langle 1|$, but not into any other (-1)-quantum coherence and not into a coherence of any other order (see Fig. 4).

The matrix representations of the superoperator blocks $\hat{\mathcal{H}}_a^{\text{comm}}$ and $\hat{\mathcal{H}}_b^{\text{comm}}$ are given by

$$\hat{\mathcal{H}}_a^{\text{comm}} = \begin{array}{cc} |C_{21}) & |C_{31}) \\ \begin{pmatrix} -\omega_k - \omega_A & \frac{1}{2}\omega_B \\ \frac{1}{2}\omega_B & -\omega_j - \omega_A \end{pmatrix} \end{array} \qquad [32]$$

and

$$\hat{\mathcal{H}}_b^{\text{comm}} = \begin{array}{cc} |C_{43}) & |C_{42}) \\ \begin{pmatrix} -\omega_k + \omega_A & -\frac{1}{2}\omega_B \\ -\frac{1}{2}\omega_B & -\omega_j + \omega_A \end{pmatrix}. \end{array} \qquad [33]$$

Relaxation superoperator. In a high magnetic field, the secular approximation allows block-diagonalization of the relaxation superoperator according to the total angular momentum of the coherences along the field

$$\hat{\Gamma} = \begin{pmatrix} \hat{\Gamma}_{+2} & & & & \\ & \hat{\Gamma}_{+1} & & & \\ & & \hat{\Gamma}_0 & & \\ & & & \hat{\Gamma}_{-1} & \\ & & & & \hat{\Gamma}_{-2} \end{pmatrix}. \qquad [34]$$

As before, the block $\hat{\Gamma}_{+2}$ is a 1×1 matrix, the block $\hat{\Gamma}_{+1}$ is a 4×4 matrix, the block $\hat{\Gamma}_0$ is a 6×6 matrix, and so on.

In the DTR model, the 4×4 block $\hat{\Gamma}_{-1}$ may be written

$$
\hat{\Gamma}_{-1} = \begin{array}{c} \quad\; |C_{21}) \quad |C_{31}) \quad |C_{43}) \quad |C_{42}) \\ \begin{pmatrix} -r_k & & & \\ & -r_j & & \\ & & -r_k & \\ & & & -r_j \end{pmatrix} \end{array}, \qquad [35]
$$

where r_j is the dephasing rate constant of coherences associated with spins in site j, and r_k is the dephasing rate constant of coherences associated with spins in site k. The inverse of these coherence dephasing rate constants are the transverse relaxation time constants T_2 of spins in the corresponding sites.

The omission of the other elements of $\hat{\Gamma}_{-1}$ corresponds to the neglect of cross-relaxation between the ^{13}C spins. This assumes that there is negligible molecular motion changing the direction or magnitude of the internuclear ^{13}C–^{13}C vector. In addition, the use of only two different relaxation rate constants in Eq. [35] implies the neglect of cross-correlation between fluctuating chemical shift anisotropy and dipolar coupling interactions (43).

With these assumptions, the Liouvillian for the (-1)-quantum coherences of the spin pair ensemble factorizes into two independent blocks, called $\hat{L}_a$ and $\hat{L}_b$, given by

$$
\hat{L}_a = -i\hat{\mathcal{H}}_a^{\text{comm}} + \hat{\Gamma}_a
$$

$$
= \begin{pmatrix} -r_k + i(\omega_k + \omega_A) & -i\frac{1}{2}\omega_B \\ -i\frac{1}{2}\omega_B & -r_j + i(\omega_j + \omega_A) \end{pmatrix} \qquad [36]
$$

and

$$
\hat{L}_b = -i\hat{\mathcal{H}}_b^{\text{comm}} + \hat{\Gamma}_b
$$

$$
= \begin{pmatrix} -r_k + i(\omega_k - \omega_A) & +i\frac{1}{2}\omega_B \\ +i\frac{1}{2}\omega_B & -r_j + i(\omega_j - \omega_A) \end{pmatrix}. \qquad [37]
$$

Suppose that the spin ensemble is characterized by a density operator $\rho(0)$ at time $t = 0$. The (-1)-quantum coherences at time $t = 0$ may be specified using the subspace kets

$$
|\rho(0))_a = \begin{pmatrix} \rho_{21}(0) \\ \rho_{31}(0) \end{pmatrix}
$$

$$
|\rho(0))_b = \begin{pmatrix} \rho_{43}(0) \\ \rho_{42}(0) \end{pmatrix}. \qquad [38]
$$

After an interval t, these coherences will have evolved into the state defined by

$$
|\rho(t))_a = \hat{V}_a(t, 0)|\rho(0))_a
$$

$$
|\rho(t))_b = \hat{V}_b(t, 0)|\rho(0))_b, \qquad [39]
$$

where the propagator $\hat{V}_a$ solves the differential equation

$$
\frac{d}{dt}\hat{V}_a(t, 0) = \hat{L}_a(t)\hat{V}_a(t, 0)
$$

$$
\hat{V}_a(0, 0) = \hat{1}_a, \qquad [40]
$$

and the unity operator for the subspace is

$$
\hat{1}_a = |C_{21})(C_{21}| + |C_{31})(C_{31}|. \qquad [41]
$$

Analogous equations apply to $\hat{V}_b$:

$$
\frac{d}{dt}\hat{V}_b(t, 0) = \hat{L}_b(t)\hat{V}_b(t, 0)
$$

$$
\hat{V}_b(0, 0) = \hat{1}_b, \qquad [42]
$$

where

$$
\hat{1}_b = |C_{43})(C_{43}| + |C_{42})(C_{42}|. \qquad [43]
$$

The solution of these equations allows the determination of the trajectories of the (-1)-quantum coherences and hence the observed NMR signal.

Analytical Peakshapes

Average Liouvillian theory. All matrix elements of $\hat{L}_a$ are periodically time-dependent. We now use average Liouvillian theory (37–39) to obtain an approximate analytical solution for the spectrum. Floquet theory could also be used (44–48).

Exact nth-order rotational resonance ($\omega_\Delta^{\text{iso}} = \omega_j^{\text{iso}} - \omega_k^{\text{iso}} = n\omega_r$) is now assumed. For simplicity, chemical shift anisotropy is ignored, and the spin–spin couplings and transverse relaxation rates are considered to be small compared to the sample rotation frequency. More general cases may be handled by the numerical simulation algorithm described in the Appendix.

The evolution in the "a" block of the (-1)-quantum subspace is described first. The Liouvillian $\hat{L}_a$ is divided into two parts,

$$
\hat{L}_a = \hat{L}_a^0 + \hat{L}_a', \qquad [44]
$$

chosen to have the matrix representations

$$
\hat{L}_a^0
$$

$$
= \begin{pmatrix} -\bar{r} + i(\bar{\omega} + \omega_A - \frac{1}{2}n\omega_r) & 0 \\ 0 & -\bar{r} + i(\bar{\omega} + \omega_A + \frac{1}{2}n\omega_r) \end{pmatrix}
$$

$$
[45]
$$

and

$$
\hat{L}_a' = \frac{1}{2}\begin{pmatrix} r_\Delta & -i\omega_B \\ -i\omega_B & -r_\Delta \end{pmatrix}. \qquad [46]
$$

These equations employ the notation

$$\bar{r} = \tfrac{1}{2}(r_j + r_k)$$
$$r_\Delta = r_j - r_k$$
$$\bar{\omega} = \tfrac{1}{2}(\omega_j + \omega_k). \qquad [47]$$

Note that the differential relaxation rate constant r_Δ may have either sign.

The subspace propagator $\hat{V}_a$ over the interval $(t, 0)$ may be written as a product of two propagators,

$$\hat{V}_a(t, 0) = \hat{V}_a^0(t, 0)\widehat{\bar{V}}_a(t, 0), \qquad [48]$$

which obey the differential equations

$$\frac{d}{dt}\,\hat{V}_a^0(t, 0) = \hat{L}_a^0(t)\hat{V}_a^0(t, 0)$$
$$\hat{V}_a^0(0, 0) = \hat{1}_a \qquad [49]$$

and

$$\frac{d}{dt}\,\widehat{\bar{V}}_a(t, 0) = \widehat{\bar{L}}_a(t)\widehat{\bar{V}}_a(t, 0)$$
$$\widehat{\bar{V}}_a(0, 0) = \hat{1}_a. \qquad [50]$$

The interaction frame Liouvillian is

$$\widehat{\bar{L}}_a(t) = \hat{V}_a^0(t, 0)^{-1}\hat{L}_a'(t)\hat{V}_a^0(t, 0). \qquad [51]$$

Since $\hat{L}_a^0$ is diagonal in the basis $\{|C_{21}\rangle, |C_{31}\rangle\}$, the propagator $\hat{V}_a^0$ is easy to evaluate:

$$\hat{V}_a^0(t, 0) = \exp\{(-\bar{r} - i\tfrac{1}{2}n\omega_r)t + i(\bar{\phi}(t, 0) + \phi_A(t, 0))\}$$
$$\times |C_{21}\rangle\langle C_{21}| + \exp\{(-\bar{r} + i\tfrac{1}{2}n\omega_r)t$$
$$+ i(\bar{\phi}(t, 0) + \phi_A(t, 0))\}|C_{31}\rangle\langle C_{31}|, \qquad [52]$$

where the dynamic phases are

$$\phi_A(t, 0) = \int_0^t dt'\,\omega_A(t')$$
$$\bar{\phi}(t, 0) = \int_0^t dt'\,\bar{\omega}(t'). \qquad [53]$$

For exact magic-angle-spinning, small through-space cou-

plings, and small CSA, these phase functions may be approximated

$$\phi_A(t, 0) \cong \pi J_{jk}t$$
$$\bar{\phi}(t, 0) \cong \bar{\omega}^{\text{iso}}t, \qquad [54]$$

where $\bar{\omega}^{\text{iso}} = \tfrac{1}{2}(\omega_j^{\text{iso}} + \omega_k^{\text{iso}})$ is the mean isotropic shift frequency of the two spins. The approximations in Eq. [54] correspond to neglect of the sideband pattern generated by the dipolar coupling and the chemical shift anisotropy.

The interaction frame Liouvillian is given by

$$\widehat{\bar{L}}_a(t) = \tfrac{1}{2}\begin{pmatrix} r_\Delta & -i\omega_B\exp\{in\omega_r t\} \\ -i\omega_B\exp\{-in\omega_r t\} & -r_\Delta \end{pmatrix}, \qquad [55]$$

which is periodic, with period $\tau_r = |2\pi/\omega_r|$. The interaction frame propagator over multiples of the period τ_r is given by the effective Liouvillian $\widehat{\bar{L}}_a$,

$$\widehat{\bar{V}}_a(N\tau_r, 0) = \exp\{\widehat{\bar{L}}_a N\tau_r\}, \qquad [56]$$

where N is an integer (37–39). The effective Liouvillian may be written in terms of a Magnus expansion

$$\widehat{\bar{L}}_a = \widehat{\bar{L}}_a^{(1)} + \widehat{\bar{L}}_a^{(2)} + \cdots, \qquad [57]$$

where the terms are given by

$$\widehat{\bar{L}}_a^{(1)} = \tau_r^{-1}\int_0^{\tau_r} dt\,\widehat{\bar{L}}_a(t)$$
$$\widehat{\bar{L}}_a^{(2)} = (2\tau_r)^{-1}\int_0^{\tau_r} dt_2 \int_0^{t_2} dt_1\,[\widehat{\bar{L}}_a(t_2), \widehat{\bar{L}}_a(t_1)], \qquad [58]$$

as in average Hamiltonian theory (49–51).

Under the conditions $|\omega_B\tau_r| \ll 1$ and $|r_\Delta\tau_r| \ll 1$, which are well-satisfied under ordinary circumstances, the Magnus expansion may be truncated at the first term, and the requirement that Eq. [56] only applies over integer multiples of the modulation period may be relaxed. The interaction frame propagator may then be written

$$\widehat{\bar{V}}_a(t, 0) \cong \exp\{\widehat{\bar{L}}_a^{(1)}t\}, \qquad [59]$$

where the matrix representation of the average Liouvillian is

$$\widehat{\bar{L}}_a^{(1)} = \tfrac{1}{2}\begin{pmatrix} r_\Delta & -i\omega_B^{(n)*} \\ -i\omega_B^{(n)} & -r_\Delta \end{pmatrix}, \qquad [60]$$

and $\omega_B^{(n)}$ is the resonant Fourier component of the spin–spin interaction, as given in Eq. [12]. Note that $\hat{\bar{L}}_a^{(1)}$ is time-independent.

The solution for the propagator $\hat{V}_a$ is completed by a diagonalization of $\hat{\bar{L}}_a$ in order to solve Eq. [59], followed by multiplication by $\hat{V}_a^0$, according to Eq. [48]. The result is

$$\hat{V}_a(t, 0) \cong \frac{\exp\{-\bar{r}t\}}{R} \begin{pmatrix} e_k^+(t)(R\cosh\frac{1}{2}Rt + r_\Delta\sinh\frac{1}{2}Rt) & +i\omega_B^{(n)*}e_k^+(t)\sinh\frac{1}{2}Rt \\ -i\omega_B^{(n)}e_j^+(t)\sinh\frac{1}{2}Rt & e_j^+(t)(R\cosh\frac{1}{2}Rt - r_\Delta\sinh\frac{1}{2}Rt) \end{pmatrix} \quad [61]$$

using the notation

$$e_j^\pm(t) = \exp\{i(\omega_j^{\text{iso}} \pm \pi J_{jk})t\}$$
$$e_k^\pm(t) = \exp\{i(\omega_k^{\text{iso}} \pm \pi J_{jk})t\}$$
$$R^2 = r_\Delta^2 - |\omega_B^{(n)}|^2. \quad [62]$$

An analogous treatment of the $\{|C_{42}), |C_{43})\}$ subspace yields the result

$$\hat{V}_b(t, 0) \cong \frac{\exp\{-\bar{r}t\}}{R} \begin{pmatrix} e_k^-(t)(\cosh\frac{1}{2}Rt + r_\Delta\sinh\frac{1}{2}Rt) & -i\omega_B^{(n)*}e_k^-(t)\sinh\frac{1}{2}Rt \\ +i\omega_B^{(n)}e_j^-(t)\sinh\frac{1}{2}Rt & e_j^-(t)(R\cosh\frac{1}{2}Rt - r_\Delta\sinh\frac{1}{2}Rt) \end{pmatrix}. \quad [63]$$

Signal detection. The quadrature-detected NMR signal may be written

$$s(t) = (Q_{\text{obs}}|\hat{V}(t, 0)|\rho(0)), \quad [64]$$

where

$$(Q_{\text{obs}}| = i(S^-|, \quad [65]$$

ignoring the receiver phase shifts (*35*). Since the two (−1)-quantum subspaces are dynamically independent, this may be written

$$s(t) = s_a(t) + s_b(t), \quad [66]$$

where

$$s_a(t) = (Q_{\text{obs}}|_a\hat{V}_a(t, 0)|\rho(0))_a \quad [67]$$

and

$$s_b(t) = (Q_{\text{obs}}|_b\hat{V}_b(t, 0)|\rho(0))_b. \quad [68]$$

The observation "bras" in the two relevant subspaces are

$$(Q_{\text{obs}}|_a = (i, i), \quad [69]$$

and

$$(Q_{\text{obs}}|_b = (i, i), \quad [70]$$

expressed in the appropriate basis sets.

Coherence transfer signals. The rotation of the sample drives coherence transfer between the spin sites during the signal detection process. We now examine the effect of this process on the spectrum.

Suppose that the spin density operator at the beginning of the detection period (defined as $t = 0$) has the form

$$\rho(0) \sim -S_{jy}. \quad [71]$$

This initial state could be produced by frequency-selective excitation, or selective cross-polarization, of the spins in site *j*. The initial spin density operator in Eq. [71] may be written

$$\rho(0) = \frac{1}{2i} C_{31} + \frac{1}{2i} C_{42} - \frac{1}{2i} C_{13} - \frac{1}{2i} C_{24}, \quad [72]$$

indicating a superposition of two (-1)-quantum and two $(+1)$-quantum coherences.

The $(+1)$-quantum coherences may be ignored if no further pulses are applied. The initial kets in the two (-1)-quantum subspaces are

$$|\rho(0))_a^j = \frac{1}{2i}\begin{pmatrix} 0 \\ 1 \end{pmatrix}$$

$$|\rho(0))_b^j = \frac{1}{2i}\begin{pmatrix} 0 \\ 1 \end{pmatrix}, \qquad [73]$$

where the superscript indicates the selective preparation of transverse magnetization of spins in sites j.

The a subspace signal in this situation is therefore

$$s_a^j(t) = s_a^{j \to j}(t) + s_a^{j \to k}(t), \qquad [74]$$

where

$$s_a^{j \to j}(t) = \tfrac{1}{2}(C_{31}|_a \hat{V}_a(t, 0)|C_{31})_a \qquad [75]$$

and

$$s_a^{j \to k}(t) = \tfrac{1}{2}(C_{21}|_a \hat{V}_a(t, 0)|C_{31})_a. \qquad [76]$$

These expressions evaluate to

$$s_a^{j \to j}(t) = \tfrac{1}{2}\exp\{i(\omega_j^{\mathrm{iso}} + \pi J_{jk})t - \bar{r}t\}$$
$$\times \left(\cosh \tfrac{1}{2}Rt - \frac{r_\Delta}{R}\sinh \tfrac{1}{2}Rt\right) \qquad [77]$$

and

$$s_a^{j \to k}(t) = \frac{i\omega_B^{(n)*}}{2R}\exp\{i(\omega_k^{\mathrm{iso}} + \pi J_{jk})t - \bar{r}t\}\sinh \tfrac{1}{2}Rt. \quad [78]$$

The corresponding b subspace signals are

$$s_b^j(t) = s_b^{j \to j}(t) + s_b^{j \to k}(t), \qquad [79]$$

with

$$s_b^{j \to j}(t) = \tfrac{1}{2}\exp\{i(\omega_j^{\mathrm{iso}} - \pi J_{jk})t - \bar{r}t\}$$
$$\times \left(\cosh \tfrac{1}{2}Rt - \frac{r_\Delta}{R}\sinh \tfrac{1}{2}Rt\right) \qquad [80]$$

and

$$s_b^{j \to k}(t) = -\frac{i\omega_B^{(n)*}}{2R}\exp\{i(\omega_k^{\mathrm{iso}} - \pi J_{jk})t - \bar{r}t\}\sinh \tfrac{1}{2}Rt. \qquad [81]$$

The "direct" signals $s_a^{j \to j}$ and $s_b^{j \to j}$ contain frequencies close to the precession frequency of spins in sites j, i.e., the frequency of the spin coherences directly excited at the beginning of the detection period. The *coherence transfer signals* $s_a^{j \to k}$ and $s_b^{j \to k}$, on the other hand, contain frequencies close to the precession frequency of spins in sites k, which were not magnetized at the start of the detection period. These spin magnetizations were generated during the detection period by mechanical transfer of coherence from sites j to sites k. The mechanical coherence transfer process leads to the appearance of NMR signal in spectral regions which are far from those directly excited by the preparation pulse sequence.

The direct signals $s_a^{j \to j}$ and $s_b^{j \to j}$ are identical, except for a frequency displacement by the J-coupling. The indirect signals $s_a^{j \to k}$ and $s_b^{j \to k}$ are also displaced in frequency by the J-coupling, but have opposite signs. The coherence transfer signals cancel out if the J-coupling is unresolved.

From Eq. [12], the phase of the coherence transfer signals depends on the molecular orientational angle γ_{MR} and the initial sample rotation angle α_{RL}^0 according to

$$\arg\{\omega_B^{(n)}(\alpha_{MR}, \beta_{MR}, \gamma_{MR})^*\} = n(\gamma_{MR} + \alpha_{RL}^0). \qquad [82]$$

If the initial density operator has the orientation-independent form given in Eq. [73], then the coherence transfer signals disappear for powder samples. The signals also disappear for unsynchronized experiments on spinning oriented samples, if extensive signal averaging is performed.

Coherence transfer signals have recently been observed experimentally on a spinning single crystal of $^{13}C_2$-labeled glycine (*52*).

A recent interpretation of the Floquet theory of NMR in rotating solids employs coherent eigenfunctions of the macroscopic rotational angular momentum (*48*). This formalism suggests an intriguing physical description of the coherence transfer signals, in terms of amplitude transfer between spatial rotational coherence and spin coherence.

Carousel average signals. If the sample is a powder, the observed signal has contributions from all possible molecular orientational angles α_{MR}, β_{MR}, and γ_{MR}. In this section, we consider the sum of signals from molecules with fixed values of α_{MR} and β_{MR} but all possible values of γ_{MR}. Such orientational subsets have been called "carousels" because the subset members have spin interactions which follow an identical cyclic trajectory as the sample is rotated, but at shifted times (*22, 53*). The carousel average signal is defined as

$$\langle s(t)\rangle_\gamma = (2\pi)^{-1}\int_0^{2\pi} d\gamma_{MR}\, s(t, \Omega_{MR}). \qquad [83]$$

The powder average signal is a superposition of contributions from separate carousels with different values of α_{MR} and β_{MR}.

Let us now assume that the initial transverse spin magnetization is excited in a frequency-independent fashion, using, for example, a strong $\pi/2$ pulse applied to thermal equilibrium magnetization or by nonselective Hartmann–Hahn cross-polarization (54). Since the coherence transfer signals $s_a^{j \to k}$ and $s_b^{j \to k}$ vanish upon carousel averaging, we only take into account the direct signals $s_a^{j \to j}$ and $s_b^{j \to j}$. The carousel average signal is given by a superposition of the four "direct" signals,

$$\langle s(t) \rangle_\gamma = \langle s_a^{j \to j}(t) + s_b^{j \to j}(t) + s_a^{k \to k}(t) + s_b^{k \to k}(t) \rangle. \quad [84]$$

For simplicity, assume that the J-coupling is small, so that the a and b contributions coincide. The carousel-average NMR signal is given by

$$\langle s(t) \rangle_\gamma = \exp\{(i\omega_j^{\mathrm{iso}} - \bar{r})t\}\left(\cosh \tfrac{1}{2}Rt - \frac{r_\Delta}{R} \sinh \tfrac{1}{2}Rt \right)$$
$$+ \exp\{(i\omega_k^{\mathrm{iso}} - \bar{r})t\}\left(\cosh \tfrac{1}{2}Rt + \frac{r_\Delta}{R} \sinh \tfrac{1}{2}Rt \right).$$
$$[85]$$

This is a convenient form for the exploration of the signal characteristics as a function of the coupling and relaxation parameters.

Two regimes of this equation may be identified, depending on the value of R, as defined in Eq. [62]. If the resonant Fourier component of the dipolar coupling $\omega_B^{(n)}$ exceeds in magnitude the transverse relaxation differential r_Δ, then the factor R is an imaginary number. This is called the regime of *slow differential damping*. If the relaxation differential r_Δ is larger than the resonant part of the coupling, then the factor R is real. This is called the regime of *fast differential damping*. The cross-over between these two regimes occurs at the *coalescence point,* in which the relaxation differential r_Δ has the same magnitude as the resonant Fourier component of the dipolar coupling $\omega_B^{(n)}$.

1. *Slow differential damping* ($|r_\Delta| < |\omega_B^{(n)}|$). The carousel average NMR signal may be written

$$\langle s(t) \rangle_\gamma = a_+\exp\{(i\omega_j^+ - \bar{r})t\} + a_-\exp\{(i\omega_j^- - \bar{r})t\}$$
$$+ a_-\exp\{(i\omega_k^+ - \bar{r})t\} + a_+\exp\{(i\omega_k^- - \bar{r})t\},$$
$$[86]$$

using the notation

$$a_\pm = \tfrac{1}{2}\left(1 \pm i\,\frac{r_\Delta}{\omega_R} \right) \quad [87]$$

and

$$\omega_j^\pm = \omega_j^{\mathrm{iso}} \pm \tfrac{1}{2}\omega_R$$
$$\omega_k^\pm = \omega_k^{\mathrm{iso}} \pm \tfrac{1}{2}\omega_R. \quad [88]$$

In these equations, the rotational resonance splitting ω_R is defined through

$$\omega_R^2 = -R^2 = |\omega_B^{(n)}|^2 - r_\Delta^2. \quad [89]$$

In the regime of slow differential dephasing, ω_R is a real number.

The NMR spectrum is obtained by Fourier transformation of the time-domain signal,

$$S(\omega) = \int_0^\infty dt\, s(t)\exp\{-i\omega t\}. \quad [90]$$

The carousel-average spectrum may therefore be written

$$\langle S(\omega) \rangle_\gamma = a_+\mathscr{L}(\omega;\, \omega_j^+, \bar{r}) + a_-\mathscr{L}(\omega;\, \omega_j^-, \bar{r})$$
$$+ a_-\mathscr{L}(\omega;\, \omega_k^+, \bar{r}) + a_+\mathscr{L}(\omega;\, \omega_k^-, \bar{r}),$$
$$[91]$$

where the Lorentzian lineshape function is

$$\mathscr{L}(\omega;\, \omega', \lambda) = \frac{1}{\lambda + i(\omega - \omega')}. \quad [92]$$

In this regime, the spectrum consists of the superposition of four Lorentzian functions, with complex amplitudes a_+ or a_- and identical peakwidths $2\bar{r}$. The center frequencies of the four Lorentzians are given by the isotropic shift frequencies ω_j^{iso} and ω_k^{iso}, plus or minus half the rotational resonance splitting ω_R.

In the limiting case of identical transverse relaxation rates $r_j = r_k$, all four peak amplitudes are real and equal. The rotational resonance splitting ω_R is equal to the magnitude of the resonant dipolar component $|\omega_B^{(n)}|$. The real part of the NMR spectrum consists of four absorption Lorentzian peaks, at the frequencies $\omega_j^{\mathrm{iso}} \pm \tfrac{1}{2}\omega_R$ and $\omega_k^{\mathrm{iso}} \pm \tfrac{1}{2}\omega_R$, with peakwidths given in rads^{-1} by $2r_j = 2r_k$. The same result is obtained by a naive analysis in which relaxation is neglected during the main body of the calculation and added afterward by imposing an exponential decay (5). The treatment given in Ref. (5) is therefore correct in the case of equal transverse relaxation rates for spins in the two sites.

In the more general situation of $r_\Delta \neq 0$, the current treatment and that given in Ref. (5) give different results. Figure 5 shows the composition of the spectrum in the case $\omega_j^{\mathrm{iso}} > \omega_k^{\mathrm{iso}}$ and $r_j + |\omega_B^{(n)}| > r_k > r_j$. Since a_+ and a_- are complex numbers, the real part of the spectrum consists of a superposition of absorption and dispersion Lorentzians. The admixture of dispersion modes causes constructive interference around the isotropic shift frequency of site j, but destructive interference around the isotropic shift frequency of site k. The result-
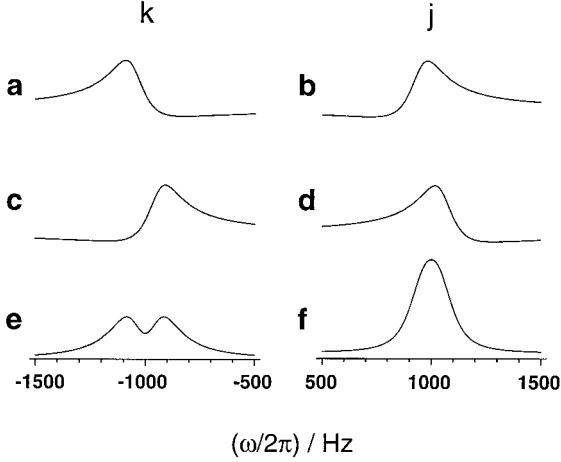
FIG. 5. (a–d) The four components of the real part of the spectrum $S(\omega)$, in the slow differential dephasing regime. (e, f) The total spectrum. The left-hand plots show the spectral region near the isotropic shift frequency of site k; the right-hand plots show the spectral region near the isotropic shift frequency of site j. The parameters are $\omega_j^{iso}/2\pi = 1000$ Hz; $\omega_k^{iso}/2\pi = -1000$ Hz; $r_j = 250$ s^{-1}; $r_k = 900$ s^{-1}; $|\omega_B^{(n)}/2\pi| = 75$ Hz.

ing spectrum shows a relatively narrow peak around the frequency ω_j^{iso} and a broad split peak around ω_k^{iso}.

2. *Fast differential damping* ($|r_\Delta| > |\omega_B^{(n)}|$). In this regime, the carousel average NMR signal is

$$\langle s(t) \rangle_\gamma = b_- \exp\{(i\omega_j^{iso} - r_-)t\} + b_+ \exp\{(i\omega_j^{iso} - r_+)t\}$$
$$+ b_+ \exp\{(i\omega_k^{iso} - r_-)t\} + b_- \exp\{(i\omega_k^{iso} - r_+)t\},$$

[93]

where

$$b_\pm = \tfrac{1}{2}\left(1 \pm \frac{r_\Delta}{R}\right)$$

[94]

and

$$r_\pm = \bar{r} \pm \tfrac{1}{2}R.$$

[95]

The quantity R is a real number in the regime of fast differential dephasing.

After Fourier transformation, the signal takes the form

$$\langle S(\omega) \rangle_\gamma = b_- \mathscr{L}(\omega; \omega_j^{iso}, r_-) + b_+ \mathscr{L}(\omega; \omega_j^{iso}, r_+)$$
$$+ b_+ \mathscr{L}(\omega; \omega_k^{iso}, r_-) + b_- \mathscr{L}(\omega; \omega_k^{iso}, r_+).$$

[96]

The spectrum is again a superposition of four Lorentzian peaks. The spectral amplitudes are real, so that the real part of the spectrum contains only absorption mode contributions. The center positions of all four peaks coincide with the isotropic shift frequencies, indicating that the rotational resonance splitting is completely quenched in this regime. Two of the four peaks have widths $2r_-$, while the other two have widths $2r_+$.

Figure 6 shows the composition of the spectrum in the case $\omega_j^{iso} > \omega_k^{iso}$ and $r_k > r_j + |\omega_B^{(n)}|$. The spectral region around the isotropic shift frequency ω_j^{iso} consists of a strong narrow Lorentzian superposed on a weak negative broad Lorentzian. Near ω_k^{iso}, a negative narrow Lorentzian and a positive broad Lorentzian are superposed. The net result is qualitatively similar to that in Fig. 5, with a narrow peak at the frequency ω_j^{iso} and a broad split peak at the frequency ω_k^{iso}.

If the relaxation differential r_Δ is reversed in sign, then the narrow unsplit peak and the broad split peak exchange position.

Figure 7 shows how the spectrum progresses from the case of slow differential dephasing to the case of fast differential dephasing as one of the relaxation rates is increased. The isotropic shift frequencies are ordered $\omega_j^{iso} > \omega_k^{iso}$. The spectral peak near the frequency ω_j^{iso} is therefore called below the "right-hand peak," while the spectral peak near the frequency ω_k^{iso} is called the "left-hand peak." In the plot shown, the right-hand transverse relaxation rate r_j is held fixed, while the left-hand rate r_k is progressively increased, starting from the case of no relaxation differential $r_j = r_k$ and ending up at the extreme differential case $r_k \gg r_j + |\omega_B^{(n)}|$. Plots a and b are in the slow differential dephasing regime, while plots d–f are in the fast differential dephasing regime. Plot c is at the coalescence point, for which $|r_\Delta| = |\omega_B^{(n)}|$.
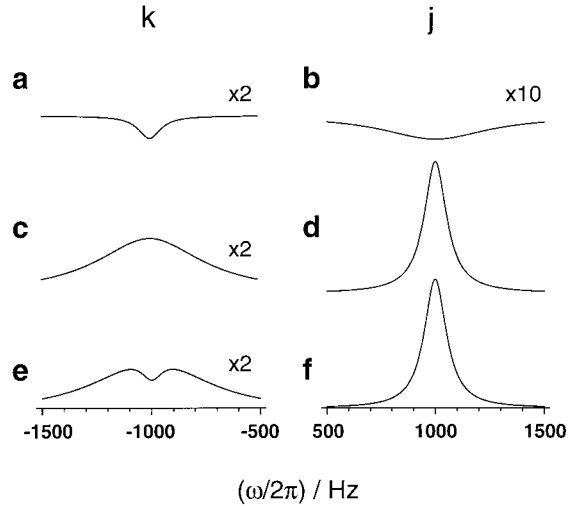

FIG. 6. (a–d) The four components of the real part of the spectrum $S(\omega)$ in the fast differential dephasing regime. (e, f) The total spectrum. The left-hand plots show the spectral region near the isotropic shift frequency of site k; the right-hand plots show the spectral region near the isotropic shift frequency of site j. The vertical scale in plots a–e are expanded by a factor of 2; the vertical scale in plot b is expanded by a factor of 10. The parameters are $\omega_j^{iso}/2\pi = 1000$ Hz; $\omega_k^{iso}/2\pi = -1000$ Hz; $r_j = 250$ s^{-1}; $r_k = 2000$ s^{-1}; $|\omega_B^{(n)}/2\pi| = 75$ Hz.
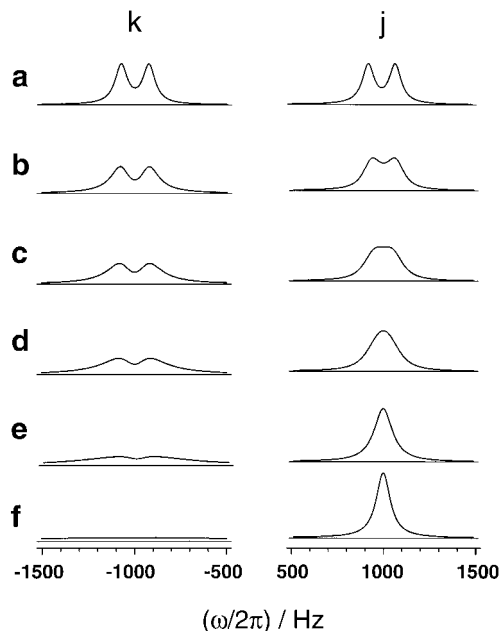
FIG. 7. Rotational resonance spectra as a function of one of the transverse relaxation rates. In all plots, the parameters are given by $\omega_j^{iso}/2\pi = 1000$ Hz; $\omega_k^{iso}/2\pi = -1000$ Hz; $r_j = 250$ s^{-1}; $|\omega_B^{(n)}/2\pi| = 75$ Hz. The transverse relaxation rate constant of the left-hand peak r_k is increased from top to bottom in the figure. (a) $r_k = 250$ s^{-1}; (b) $r_k = 500$ s^{-1}; (c) $r_k = 721$ s^{-1}; (d) $r_k = 1000$ s^{-1}; (e) $r_k = 2000$ s^{-1}; (f) $r_k = 5000$ s^{-1}. Plot c is at the coalescence point.

Figure 7a shows four resolved Lorentzians, of equal widths, with a rotational resonance splitting corresponding to the resonant dipolar Fourier component $|\omega_B^{(n)}|$. As the decay rate associated with the *left-hand peak* r_k is increased, the splitting on the *right-hand peak* gradually collapses, and all peaks broaden. At the coalescence point $|r_j - r_k| = |\omega_B^{(n)}|$ (Fig. 7c), the rotational resonance splitting disappears on the right-hand peak, although the splitting persists on the left-hand peak.

When the rate r_k is increased further, the left-hand peak becomes broader, while the right-hand peak becomes narrower. For very large decay rates r_k, the left-hand peak essentially vanishes, while the width of the right-hand peak is reduced until it attains the limiting value $2r_j$ set by the corresponding decay rate constant.

The integrals of both spectral peaks are constant throughout this progression.

The behavior of the right-hand spectral peak in Fig. 7 resembles the case of two-site chemical exchange (55–58). Indeed, the mathematical forms of the rotational resonance peakshapes and the symmetrical two-site exchange peak shapes are identical. The behavior of the left-hand peak, on the other hand, is more unusual. Related effects have been observed for strongly coupled two-spin systems in isotropic liquids, in the presence of rapid transverse relaxation of one of the coupled sites (56–60). The phenomena described in this paper are more striking because rotational resonance induces "strong

coupling," even when the isotropic shift frequencies are widely separated.

The process sketched in Fig. 7 may be interpreted as a form of *self-decoupling by rapid transverse relaxation.* This is an unusual NMR phenomenon. It was observed many years ago in the liquid-state NMR of coupled spin systems which are in chemical exchange with paramagnetic species (60).

Transverse self-decoupling should not be confused with similar phenomena involving longitudinal relaxation. For example, rapid spin–lattice relaxation of a coupling partner is well-known to cause collapse of the spin–spin splitting. This has been termed "scalar relaxation of the second kind" by Abragam (61). This mechanism is independent of the *transverse* relaxation of the coupling partner.

Another related effect involves decoupling by *rapid cross-relaxation* of the coupling partner with one or more additional spins. In solid-state NMR, self-decoupling arises when the coupling partner is involved in a rapid exchange of longitudinal spin magnetization with homonuclear coupling partners (62–67). In solution NMR, longitudinal cross-relaxation of the coupling partner has been shown to cause a partial collapse of spectral splittings (68). These phenomena should be strongly distinguished from the transverse self-decoupling phenomenon described in this paper, which does not require magnetization exchange or cross-relaxation.

DTR Powder Simulations

The analytical expressions given above ignore chemical shift anisotropy and *J*-couplings and only involve an average over the single Euler angle γ_{MR}. We have performed realistic spectral calculations by using a variant of the COMPUTE algorithm (20–23) to integrate the Liouville equations of motion, Eqs. [40] and [42], including all relevant spin interactions. A description of the L-COMPUTE algorithm, suitable for Liouville space calculations, is given in the Appendix.

Figure 8 shows some realistic L-COMPUTE simulations of 11,20-^{13}C$_2$-all-*E*-retinal at the $n = 1$ rotational resonance in a magnetic field of 9.402 T. These simulations are full powder averages, using the estimated chemical shift and spin coupling parameters specified in Ref. (69). The simple DTR model is used in these simulations. The C11 and C20 sites are assigned different transverse relaxation rate constants r_{11} and r_{20}, which are assumed to be uniform for the whole sample and independent of orientation.

The simulations shown in Fig. 8 have the same value for r_{20}, while the value of r_{11} increases on progressing down the figure. The other simulation parameters are described in Ref. (69).

Note that the increase in the C11 transverse relaxation rate r_{11} has the most dramatic effect on the C20 peak. At rapid C11 relaxation rates, the C20 peak loses the rotational resonance splitting and assumes a tent-like shape. At the same time, the base of the C11 peak is broadened, and the splitting becomes slightly deeper. These phenomena are qualitatively similar to the experimental results in Fig. 2c.
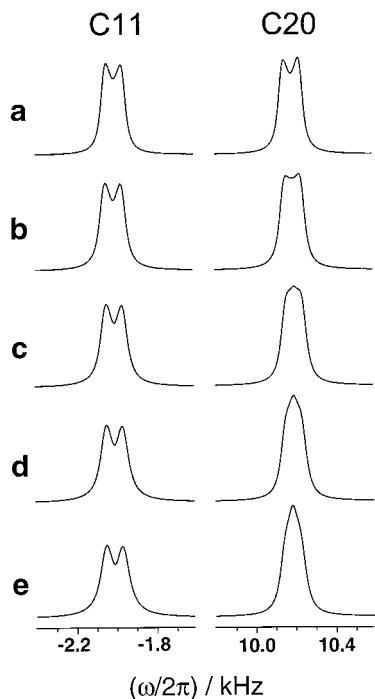
FIG. 8. Simulated powder average rotational resonance spectra of 11,20-$^{13}C_2$-all-E-retinal. The simulation parameters are given in Ref. (*69*). The transverse relaxation rate constant for the C20 site is equal to $r_{20} = 126 \ s^{-1}$ throughout. The transverse relaxation rate constant for the C11 site is given by (a) $r_{11} = 126 \ s^{-1}$; (b) $r_{11} = 157 \ s^{-1}$; (c) $r_{11} = 189 \ s^{-1}$; (d) $r_{11} = 220 \ s^{-1}$; (e) $r_{11} = 251 \ s^{-1}$.

The qualitative agreement between these calculations and the experimental RR spectrum is encouraging. However, a full explanation must pass a more rigorous test. It should be possible to use the same parameters to explain the spectra both on and off rotational resonance. In particular, the narrow spectral peaks off rotational resonance must be explicable.

The simple DTR model does not quite pass this test. In order to obtain good agreement with the experimental spectrum at rotational resonance, one must use a relaxation parameter r_k for the C11 site equal to ~250 s^{-1}. When the simulations are run with the same parameters off rotational resonance, the result is a C11 peak which is too broad by a factor of around 2.

MDTR Model

The weak point in the DTR formulation is the representation of the residual ^1H–^{13}C interactions by an oversimplified relaxation model. The treatment may be made more realistic by taking into account the nonexponentiality of the ^{13}C transverse relaxation. The slightly broad base of the C11 peak in Fig. 3c is experimental evidence of this nonexponentiality.

Abragam (*61*) has shown that in dipolar coupled systems, molecular motion causes a transition from a Gaussian-like free

induction decay (in the case of slow motion) to an exponential decay (in the case of fast motion). Some models of nonexponential relaxation in the intermediate regime were also explored (*61*). In polymer science, nonexponential relaxation models such as the Kohlrausch–Williams–Watts "stretched exponential" are widely used (*70*). These models might be applicable to the problem of imperfect heteronuclear decoupling, since it may be argued, at least qualitatively, that spin diffusion within the abundant spin system has a similar effect to molecular motion; the spin polarizations are exchanged, instead of the molecular positions.

It is difficult to apply these more sophisticated relaxation models to the present problem, since they cannot be accomodated within the framework of the Liouville–von Neumann equation (Eq. [18]), which is linear, first-order, and homogeneous.

In this paper, we take the nonexponentiality of the transverse relaxation into account in a crude way. The results of two separate DTR calculations, using different pairs of transverse relaxation rates, are superimposed. We call this the *multiple differential transverse relaxation model.*

Our choice of this model is dictated by practical considerations—it is the simplest model which is nonexponential and yet which may be readily simulated. Nevertheless, recent work on the decoupling problem suggests that there may also be some theoretical basis for this approach, at least on a qualitative level.

A number of workers have examined the problem of heteronuclear spin decoupling in the presence of magic-angle spinning (*24–32*). It is widely recognized that heteronuclear decoupling becomes less effective at high spinning frequencies, due to destructive interference between the decoupling field and the sample rotation. Particularly strong effects are observed in systems containing isolated heteronuclear spin pairs, where the application of a RF field to one of the spin species causes a strong *recoupling* effect, if a rotary resonance condition is satisfied (*29, 30*). Normally, this first-order recoupling effect occurs in the presence of rather weak RF fields.

Recently, Ernst and co-workers (*71*) investigated *second-order recoupling* effects which occur in the presence of strong RF fields. These authors identified the chemical shift anisotropy of the irradiated spins as a mechanism of second-order recoupling. The treatment predicts a ~100-Hz splitting for the ^{13}C peaks of magnetically isolated CH groups, under typical magic-angle spinning conditions and strong proton decoupling.

Broadenings of this magnitude are rarely observed in the ^{13}C NMR of typical organic materials. Ernst and co-workers (*71*) pointed out that in most cases, the second-order recoupling effects are quenched by rapid spin diffusion among the abundant spins. The partially decoupled ^{13}C peak shapes of adamantane could be explained by using a kinetic exchange matrix to model the ^1H–^1H spin diffusion process (*67*). This is a relatively simple case, in which none of the interactions are strongly anisotropic.

Let us speculate on an extension of the kinetic exchange model of Ernst *et al.* (*67*) to the case of typical strongly coupled organic solids. In these systems, the importance of ^{1}H–^{1}H spin diffusion for good heteronuclear decoupling has been supported by a variety of experimental observations (*26–28, 62–64*). Consider the case of a ^{13}C spin with a strong dipolar coupling to a single neighboring ^{1}H spin, which participates in a network of couplings to other protons. This is the situation for the C11 site in sample **I**. The cross-relaxation of the directly bonded proton with the neighboring protons may be modeled through a stochastic exchange process for the proton between the two Zeeman states $|+\frac{1}{2}\rangle$ and $|-\frac{1}{2}\rangle$. The solutions of such kinetic treatments have a well-known form (*58*): For rapid exchange between two sites, the spectra have the form of two superimposed Lorentzians, one broad and one narrow. If the exchange rate is very fast, the broad component is weak, and a single narrow Lorentzian survives. If the exchange rate is relatively slow, the broad component is more prominent, and the relaxation is visibly biexponential. These results hold for fast exchange rates, beyond the "coalescence point."

This biexponential behavior is already suggestive of the MDTR model of the ^{13}C transverse relaxation. Furthermore, the kinetic exchange model of decoupling suggests a possible rationalization of the static field dependence and/or spinning frequency dependence of the RR spectra.

When the static magnetic field is increased, the ^{1}H chemical shifts and shift anisotropies become larger, in frequency units. This increases the second-order recoupling effect, which involves a combination of ^{1}H chemical shift anisotropies and ^{1}H–^{13}C dipolar interactions. In addition, the increased ^{1}H isotropic chemical shift dispersion is expected to attenuate the ^{1}H–^{1}H spin diffusion, which appears as an exchange rate in the kinetic model. Furthermore, a higher static field requires a corresponding increase in the spinning frequency if rotational resonance is to be maintained. Faster spinning is also expected to slow down the ^{1}H–^{1}H spin diffusion. All of these effects pull in the same direction—from the "fast exchange regime," where the relaxation is expected to be purely exponential, to the neighborhood of the coalescence point, where the transverse relaxation becomes strongly biexponential.

The kinetic exchange model of spin decoupling suggests that high static magnetic fields and/or spinning frequencies cause a markedly increased nonexponentiality of the transverse ^{13}C relaxation.

The kinetic model sketched above is expected not to hold for methylene (CH$_2$) groups, in which the ^{13}C spin is strongly coupled to two protons, which have a strong mutual homonuclear coupling. There is experimental evidence that CH$_2$ groups behave rather differently and have significantly nonexponential transverse relaxation even at moderate fields and spinning frequencies (see below).

Although these arguments are speculative at present, they do seem to point toward a qualitative explanation of the ^{13}C
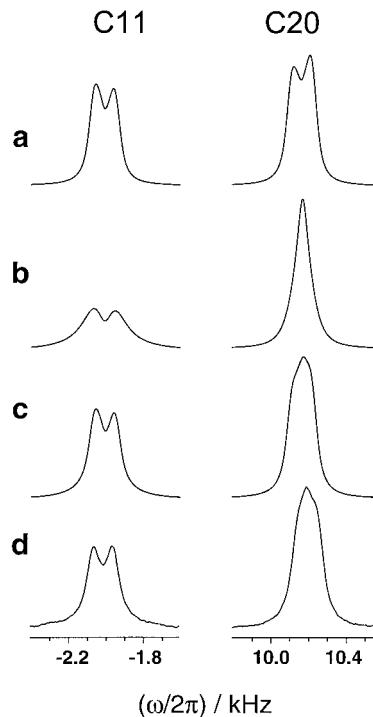

FIG. 9. Rotational resonance spectra of 11,20-^{13}C$_2$-all-*E*-retinal. (a) Simulation using relaxation rate constants $\{r_{11}, r_{20}\} = \{126$ s^{-1}, 113 s$^{-1}\}$; (b) Simulation using relaxation rate constants $\{r_{11}, r_{20}\} = \{503$ s^{-1}, 113 s$^{-1}\}$; (c) Superposition of simulation a (weight 0.67) and simulation b (weight 0.33). (d) Experimental spectrum of **I**, corrected for natural abundance signals.

rotational resonance spectra, including the static field dependence. At the moment, we have simply used the MDTR model in an empirical fashion, adjusting the relevant parameters to obtain a reasonably consistent treatment.

Some MDTR powder simulations are presented in Fig. 9. Figure 9a shows a simulated RR spectrum obtained with similar values for the transverse relaxation rate constants of the two sites. Since the relaxation differential is small, the rotational resonance splitting is clearly displayed for both peaks. Figure 9b shows a simulated RR spectrum obtained with a strong relaxation differential for the two sites ($r_{11} = 503$ s^{-1}; $r_{20} = 113$ s^{-1}). The C20 peak displays no RR splitting in this case. By superposing these two subspectra (Fig. 9c), with relative weights of 2:1, one obtains a simulation which is in rather good agreement with the experimental RR spectrum (Fig. 9d). The triangular form of the C20 peak is rather well-reproduced, as well as the broad base of the C11 peak.

Crucially, the same MDTR parameters provide good agreement with experiments off rotational resonance. Figure 10 shows a set of simulations and experimental spectra at a spinning frequency $\omega_r/2\pi = 10.000$ kHz. The simulated and experimental peaks have comparable widths, and the broad base of the experimental C11 peak is reproduced well in the simulation.
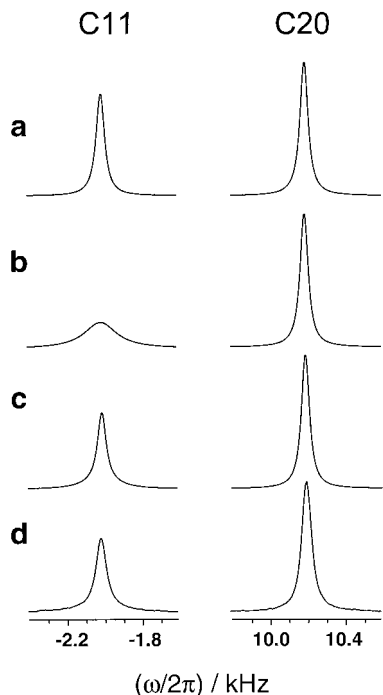
C11   C20

a

b

c

d

-2.2   -1.8   10.0   10.4

$(\omega/2\pi)$ / kHz

FIG. 10. Spectra for 11,20-^{13}C$_2$-all-E-retinal, at a spinning frequency $\omega_r/2\pi = 10$ kHz (well off rotational resonance). (a) Simulation using relaxation rate constants $\{r_{11}, r_{20}\} = \{126$ s^{-1}, 113 s$^{-1}\}$; (b) Simulation using relaxation rate constants $\{r_{11}, r_{20}\} = \{503$ s^{-1}, 113 s$^{-1}\}$; (c) Superposition of simulation a (weight 0.67) and simulation b (weight 0.33). (d) Experimental spectrum of **I**, corrected for natural abundance signals.

Modulated Decoupling

If this explanation has any merit, then the RR spectra should be sensitive to modulated decoupler schemes which change the decoupling characteristics at high spinning frequencies. For example, the popular TPPM scheme has been reported to increase apparent peak *integrals* as well as peak heights at high spinning frequencies (*31*). This may only be explained if the partially decoupled peaks have very broad bases which easily escape notice in the usual spectrum and which are reduced by TPPM decoupling.

TPPM decoupling does indeed have a strong effect on the RR peakshapes of **I**. The spectrum shown in Fig. 11b was obtained at 9.402 T with TPPM proton decoupling. The proton decoupler field corresponded to a nutation frequency of 82 kHz. The phase of the decoupler field was switched between the values $\pm22.5°$ every 7 μs. A barely resolved splitting is obtained on the C20 peak under these conditions. We were again able to simulate the experimental spectrum quite well by superposing two DTR subspectra. The simulation shown in Fig. 11a employed the same pair of simulations as used in Figs. 9a and 9b, but with weights of 6.7:1.

Increasing the amplitude of the CW decoupler field, without introducing phase modulation, changed the RR peak shapes gradually. However, the available decoupler level (up to 100

kHz nutation frequency) was insufficient to achieve ideal RR peakshapes.

IV. ALTERNATIVE EXPLANATIONS

The above model was formulated only after considering many other explanations, all of which we could rule out by further experimental tests and other evidence. In this section, we sketch briefly a number of postulated mechanisms and our reasons for rejecting them.

It should be recalled that a successful explanation must be consistent with the following observations: (i) narrow spectral peaks are obtained off rotational resonance; (ii) the two RR peaks have a very different form, with one peak split and the other unsplit; and (iii) the RR spectra are field-dependent—for the labeled retinal, peakshape anomalies are observed at 9.402 T but not at 4.702 T. This apparent field-dependence could also be a disguised dependence on the spinning frequency, since when the magnetic field is doubled, the spinning frequency must also be doubled to maintain the RR condition.

Isotopic Impurities

Defects in the isotopic distribution, such as an excess of the C20 label, could perturb the right-hand peak in Fig. 2c. This possibility was eliminated by mass spectroscopy and solution NMR, as well as by the absence of the RR anomalies at 4.702 T.

Intermolecular ^{13}C–^{13}C Interactions

In isotopically nondiluted material, homonuclear interactions between ^{13}C spins on different molecules are known to perturb the rotational resonance peak shapes. We eliminated this possibility by using a sample in which the ^{13}C$_2$-labeled molecules were diluted in nonlabeled material.

At a field of 9.402 T, the RR peak shapes of nondiluted 98% all-E-retinal have a similar form as for the diluted sample, but with a superimposed additional broadening. The spectrum of

C11   C20

a

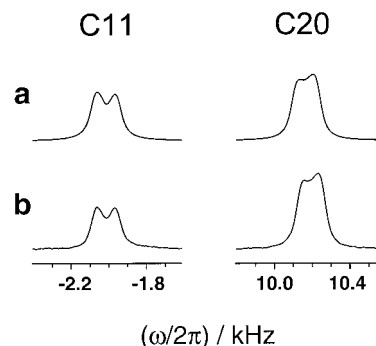**b**

-2.2   -1.8   10.0   10.4

$(\omega/2\pi)$ / kHz

FIG. 11. Rotational resonance spectra of 11,20-^{13}C$_2$-all-E-retinal, in the presence of TPPM decoupling (experimental parameters given in the text). (a) Superposition of the simulation in Fig. 9a (weight 0.87) and Fig. 9b (weight 0.13). (b) Experimental spectrum of **I**, corrected for natural abundance signals.

nondiluted 98% all-*E*-retinal at a field of 4.702 T has been discussed in Ref. (*8*).

Isotropic Shift Dispersion

Rotational resonance peak shapes which disagree with simple spin-pair simulations have been reported before (*11, 17, 72*). However, in most of these cases, the sample had a dispersion of isotropic chemical shift values, due to imperfect crystallinity, inhomogeneous hydration, or a distribution of molecular conformations. A spread in chemical shifts causes some of the spin pairs to be off rotational resonance, unless the two isotropic chemical shifts are perfectly correlated (as occurs, for example, in the case of susceptibility broadening). It is possible to contrive shift distribution models which reproduce the anomalous spectral appearance shown in Fig. 2c.

However, in order to explain the anomalous RR peakshapes, it is necessary to invoke an isotropic chemical shift distribution which is quite broad (about 50 Hz in frequency units). Such a shift distribution would be highly visible in the off RR spectra, which is not the case.

Spinning Axis Errors

The angle β_{RL} between the spinning axis and the static field should be equal to the "magic angle" arctan $\sqrt{2}$. A misset from this angle broadens the NMR peaks by an amount proportional to $3 \cos^2\beta_{RL} - 1$ multiplied by the shift anisotropy. Simulations show that an angle misset of around 0.4° gives rise to effects which are qualitatively similar to those shown in Fig. 2c.

However, a misset spinning axis would lead to broad peaks off RR, which is not the case. This mechanism was definitively ruled out by taking a set of NMR spectra as a function of spinning axis angle β_{RL}, bracketing the magic angle in very small steps. It proved to be impossible to remove the peak shape anomalies by adjusting the spinning angle.

Spinning Frequency Fluctuations

The experimental spinning frequency was stabilized to about ±2 Hz. Simulations show that fluctuations in the spinning frequency of this magnitude do not perturb the peak shapes significantly. Larger fluctuations do perturb the theoretical peak shapes, but always in such a way as to lead to *symmetrical* perturbations of the two spectral peaks (i.e., the two peaks appear as near mirror images of each other).

The experimental shapes of the two peaks are very different, so this explanation was rejected.

Uncertain Chemical Shift Tensors

Simulations of rotational resonance spectra require knowledge of the magnitude and orientations of the chemical shift anisotropy tensors. Uncertainty in the CSA principal values and orientations could be a source of error.

Simulations show that the peak shapes at the $n = 1$ RR are very insensitive to changes in the tensors. In addition, the small peak shape changes which are induced by large modifications of the CSA tensors are always nearly symmetrical for the two peaks, in disagreement with the observed effects.

Molecular Motion

There is no evidence for significant molecular motion on a time scale which might disturb the rotational resonance phenomenon. The peak shapes off RR are very narrow. The ^{13}C spin–lattice relaxation time constants are long (several seconds).

Nonsecular Effects

There have been several reports of small effects whose interpretation requires a correction to the usual secular form of the spin Hamiltonian in high magnetic field (*73–76*). Kundla and Lippmaa (*73*) analyzed rotational resonance spectra in the presence of nonsecular perturbations and predicted various field-dependent peak shape phenomena.

However, these nonsecular effects are only of the order of a few Hertz under the conditions described here. They are too small to explain the observed anomalies.

Indirect Spin–Spin Coupling

The isotropic *J*-coupling between the C11 and C20 spins is known from solution NMR and is very small (less than 3 Hz). Simulations indicate that it cannot explain the observed anomalies.

In principle, the rank 1 and rank 2 parts of the indirect spin–spin coupling should also be considered. If these terms were very large (~100 Hz), simulations show that both could perturb the RR spectra significantly. However, such large indirect spin–spin interactions are physically implausible. Furthermore, the spectral effects are predicted to be symmetrical for the two peaks. In addition, this mechanism cannot explain the field-dependence.

V. DISCUSSION

To summarize, we propose that the anomalies in the rotational resonance ^{13}C spectra of 11,20-^{13}C$_2$-all-*E*-retinal are caused by the following factors: (i) the ^{13}C transverse relaxation is augmented by imperfect decoupling of abundant spins; (ii) this transverse relaxation is nonexponential, especially at high spinning frequencies and/or high magnetic fields, and (iii) the dynamics of coupled spins at rotational resonance are strongly affected by this perturbed transverse relaxation, particularly by fast-relaxing components which easily escape notice in a spectrum taken off rotational resonance.

These peak shape anomalies have the feature that small decoupling imperfections for one of the coupled sites tend to perturb most strongly the peak associated with the *other* site.
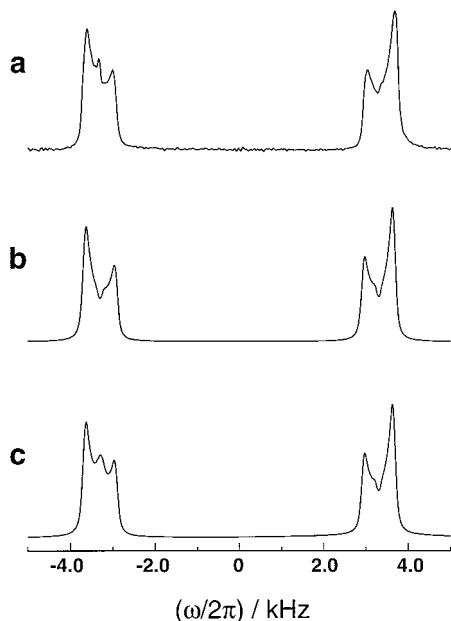
FIG. 12. ^{13}C spectra of 98% [1,2-$^{13}C_2$, ^{15}N]-glycine at a field of 4.702 T, on the $n = 1$ rotational resonance condition ($\omega_r/2\pi = 6.660$ kHz). The spectral regions near the C1 and C2 centerbands are shown. (a) Spectrum of 98% [1,2-$^{13}C_2$, ^{15}N]-glycine (16 acquired transients). The spectrum was obtained on a Chemagnetics CMX-400 spectrometer, using a 4-mm zirconia rotor. (b) Conventional simulation of (a), using the parameters given in Ref. (77). The effect of the ^{15}N spin is ignored. (c) Liouville space spectral simulation. A MDTR model is used with two pairs of relaxation parameters: $\{r_{C2}, r_{C1}\} = \{0.28, 0.28\} \times 10^3$ s^{-1} (weight 0.76), and $\{r_{C2}, r_{C1}\} = \{10.3, 0.28\} \times 10^3$ s^{-1} (weight 0.24).

Roughly speaking, rapid transverse relaxation of one of the sites takes those spins out of rotational resonance and narrows the spectral peak associated with the coupled site.

We have produced a Liouville space theory of rotational resonance in the presence of exponential transverse relaxation, which explains the qualitative features of the anomalous peak shapes. Good agreement with experiment is obtained by taking into account the nonexponentiality of the transverse relaxation. We have used a simple model in which two simulations with different pairs of relaxation parameters are superposed.

These rotational resonance effects are not restricted to exotic samples. Consider, for example, the RR spectrum of 98% [1,2-$^{13}C_2$, ^{15}N]-glycine, obtained from Cambridge Isotope Laboratories (Andover, MA) and used without further purification or recrystallization. The $n = 1$ RR spectrum shown in Fig. 12a was obtained at a static magnetic field of 4.702 T, a spinning frequency of $\omega_r/2\pi = 6.600$ kHz, and a proton decoupler field corresponding to a nutation frequency of 81 kHz. The less-shielded (left-hand) spectral peak, associated with the C1 (carboxylate) carbons, shows a sharp central feature, which is not reproduced in the conventional RR simulation, based on an isolated spin-pair model (Fig. 12b). (The ^{15}N spin is not expected to perturb the ^{13}C peaks significantly, and is neglected in the simulation.) This sharp feature may be due in part to

signals from the minor 1-^{13}C isotopomer; however, the abundance of this isotopomer is too low to explain the peak completely. The model discussed above explains the anomalous form of the C1 peak in terms of decoupling imperfections for the C2 (methylene) site. A MDTR simulation, using the spin interaction parameters given in Ref. (77), is shown in Fig. 12c. The general features of the experimental spectrum are reproduced qualitatively. Better agreement could presumably be obtained by adding more MDTR components and allowing for minor isotopomeric contributions.

In the case of 98% [1,2-$^{13}C_2$, ^{15}N]-glycine, the RR spectral anomalies appear even under "mild" conditions (low static field and low spinning frequency). We do not understand this behavior at the moment, but it may be associated with the special features of spin dynamics in a CH_2 group, in which two strongly coupled protons interact with the same ^{13}C spin.

Even zinc $^{13}C_2$-acetate, which is widely used as a model compound for rotational resonance studies, often displays small spectral anomalies. It is rather usual to obtain a "bump" near the middle of the less-shielded C1 (carboxylate) peak. An example may be found in Fig. 7e of Ref. (5). This bump has sometimes been attributed to isotopic impurities, but it seems likely that this feature is really due to imperfect decoupling of the protonated C2 (methyl) site.

The treatment given here also predicts the existence of RR spectral anomalies in other circumstances. For example, chemical exchange processes, or unresolved homonuclear couplings, selectively accelerate the transverse relaxation of spins in particular sites and should cause similar spectral perturbations at rotational resonance. The extreme sensitivity of the RR spectra to differential transverse relaxation may be useful for studying such weak broadening mechanisms.

Finally, we would like to address two further issues: (i) what do these results mean for the quantitative application of RR in molecular structure determination, and (ii) what implications do these results have in the wider NMR context?

Two different RR effects are commonly used in biomolecular structural studies: longitudinal magnetization exchange and one-dimensional RR spectra. The implications for RR spectra are addressed first.

Clearly, the above conclusions imply that rotational resonance spectra must be used with the utmost caution as a source of molecular structural information. The spectra are sensitive to details of the transverse relaxation which are not under complete control and which are hard to quantitate accurately. Equations such as Eq. [89] indicate that the spectral splitting is sensitive to the transverse relaxation differential between the coupled sites, as well as the structurally significant magnetic dipole–dipole coupling.

Nevertheless, this may not rule out structural applications of RR spectra, at least in some cases. As emphasized above, the most profound perturbations tend to occur on only one of the two peaks. Verdegem *et al.* (13) studied the observed RR splittings in a series of labeled retinals, taking into account

only the split peak, and found a good semi-empirical relation between the splitting and the dipole–dipole couplings estimated from the X-ray structure. The validity of this semi-empirical approach relies on having comparable ^{13}C–^{1}H dipolar field environments for both model compound and target. More simulation work using the new theory is necessary to determine whether this approach could be useful in general applications.

A new method for efficient double-quantum filtering of rotational resonance spectra has recently been described (78). This filtering scheme greatly reduces the spectral anomalies (as well as eliminating background signals), and may simplify the quantitative interpretation of RR spectra.

The implications of the new analysis for *longitudinal magnetization exchange* at rotational resonance are less severe. Longitudinal magnetization transfer has been analyzed with a Liouville space approach for many years (5), so the present work holds few surprises in this regard. However, it appears that even RR magnetization exchange studies must be more attentive to the *nonexponentiality* of the transverse relaxation, especially at high magnetic fields/spinning frequencies. At least two exponential decay components may be needed to model the zero-quantum relaxation. Recent direct measurements of zero-quantum relaxation have indicated nonexponential decay, in some circumstances (7).

Methods have been developed which are less sensitive to the value of the zero-quantum relaxation rate constant (9). Hopefully, these methods are also less sensitive to the nonexponentiality of the zero-quantum relaxation.

The theoretical analysis given above predicts the existence of coherence transfer signals at rotational resonance. These signals are caused by mechanically induced coherence transfer from one set of spins to the other during the acquisition of the NMR signal. The existence of such signals is a matter for concern, since it challenges the common assumption that the integrated amplitude of a given spectral peak faithfully represents the magnetization of just one set of spins at the beginning of signal detection. The analysis given above shows that this assumption is safe. The integral of the coherence transfer signals cancels out, and the signals themselves disappear for powder samples, in simple experimental situations.

Turning now to the wider implications, the present work indicates that it is very difficult, with current technology, to dynamically isolate dilute spins from an abundant spin matrix, especially in the case of high static fields and/or magic-angle spinning frequencies. A more sophisticated theory of spin decoupling under high field/fast MAS conditions, as well as improved decoupling methodology, is needed. The residual contacts between dilute spins and abundant spins may have subtle and unexpected effects on solid-state NMR spectra, which do not always correspond to a simple broadening of the NMR peaks. These anomalies are expected to become more widespread as static magnetic fields and spinning frequencies continue to increase.

APPENDIX

The L-COMPUTE Algorithm

In this Appendix, we describe the L-COMPUTE algorithm used for the simulations. This is an extension of the COMPUTE algorithm used for fast Hilbert space calculations of periodic systems (20–23). Liouville space calculations require a modified algorithm, since the propagators are not unitary in general.

In the discussion below, the integers j and k no longer represent spin site labels. They are used instead to index time and frequency domain components, as in Ref. (20).

Suppose that the nuclear spins are subjected to a periodic Liouvillian $\hat{L}(t)$, with period T. This may be represented as a repeating sequence of n piecewise time-independent Liouvillians $\hat{L}_1\hat{L}_2 \ldots \hat{L}_n\hat{L}_1\hat{L}_2 \ldots$, each Liouvillian being applied over a time interval $\tau = T/n$, i.e.,

$$\hat{L}(t) = \hat{L}_j \quad \text{if } (j-1)\tau < t \leq j\tau \qquad [97]$$

and

$$\hat{L}_{j+n} = \hat{L}_j. \qquad [98]$$

The case of continuously varying Liouvillians may be handled by increasing n indefinitely.

The Liouville space propagator for the jth interval is denoted

$$\hat{S}_j = \exp\{\hat{L}_j\tau\}, \qquad [99]$$

so that the sequence of propagators $\hat{S}_j$ has the same periodicity as the sequence of Liouvillians,

$$\hat{S}_{j+n} = \hat{S}_j. \qquad [100]$$

The accumulated propagator over the first j intervals is denoted by

$$\hat{A}_j = \hat{S}_j \ldots \hat{S}_2\hat{S}_1, \qquad [101]$$

implying the property

$$\hat{A}_{j+n} = \hat{A}_j\hat{A}_n. \qquad [102]$$

The numerical algorithm starts by diagonalizing the locally time-independent Liouvillians $\hat{L}_j$ in order to estimate the element propagators $\hat{S}_j$. The matrix representations of the individual propagators are multiplied together to obtain the set of accumulated propagators $\hat{A}_j$ and the full period propagator $\hat{A}_n$.

The period propagator $\hat{A}_n$ is not unitary in general. Diagonalization of $\hat{A}_n$ leads to a set of eigenvalues ν_s, a set of *right eigenkets* $|Q_s^R\rangle$, and a set of *left eigenbras* $\langle Q_s^L|$, defined as

$$\hat{A}_n|Q_s^R) = v_s|Q_s^R)$$

$$(Q_s^L|\hat{A}_n = (Q_s^L|v_s. \qquad [103]$$

The operators $|Q_s^R)$ and $(Q_s^L|$ are estimated in practice by numerical diagonalization of $\hat{A}_n$:

$$\hat{A}_n = \hat{X}\hat{V}\hat{X}^{-1}, \qquad [104]$$

where $\hat{V}$ is a diagonal matrix, with elements v_s. The right eigenkets $|Q_s^R)$ are the columns of $\hat{X}$, and the left eigenbras $(Q_s^L|$ are the rows of $\hat{X}^{-1}$. In general, the set of operators Q_s^R is not orthogonal. The set of operators Q_s^L is also not orthogonal. However, the right eigenkets are orthogonal to the left eigenbras:

$$(Q_r^L|Q_s^R) = \mathrm{Tr}\{Q_r^{L\dagger}Q_s^R\} = \delta_{rs}. \qquad [105]$$

This makes it possible to write the unity superoperator in the following way:

$$\hat{1} = \sum_s |Q_s^R)(Q_s^L|. \qquad [106]$$

By taking the logarithm of the eigenvalues v_s, and dividing by the period T, we obtain the eigenvalues of the *effective Liouvillian*, denoted z_s,

$$z_s = T^{-1}\log v_s. \qquad [107]$$

The period propagator may then be written

$$\hat{A}_n = \sum_s \exp\{z_s T\}|Q_s^R)(Q_s^L|. \qquad [108]$$

The effective Liouvillian eigenvalues z_s are complex numbers in general.

Suppose that the initial density operator corresponds to the superket $|\rho(0))$ and the observable operator to the superbra $(Q_{\mathrm{obs}}|$. It proves to be convenient to introduce the following *excitation and detection coefficients:*

$$\mathcal{E}_s^j = (Q_s^L|\{\hat{A}_j\}^{-1}|\rho(0))\exp\{+z_s j\tau\}$$

$$\mathcal{D}_s^j = (Q_{\mathrm{obs}}|\hat{A}_j|Q_s^R)\exp\{-z_s j\tau\}. \qquad [109]$$

These are calculated for time points $j = 1, 2 \ldots n$ within one period by straightforward matrix/vector multiplications. Both sets of coefficients are periodic

$$\mathcal{E}_s^{j+n} = \mathcal{E}_s^j$$

$$\mathcal{D}_s^{j+n} = \mathcal{D}_s^j \qquad [110]$$

and may be written as discrete Fourier series, with Fourier coefficients denoted ϵ_s^k and δ_s^k:

$$\mathcal{E}_s^j = \sum_{k=-n/2+1}^{n/2} \epsilon_s^k \exp\{i2\pi jk/n\}$$

$$\mathcal{D}_s^j = \sum_{k=-n/2+1}^{n/2} \delta_s^k \exp\{i2\pi jk/n\}. \qquad [111]$$

Numerically, the Fourier coefficients ϵ_s^k are calculated by evaluating the sets of periodic factors $\mathcal{E}_s^j$, followed by a fast Fourier transform. A similar calculation is performed to evaluate the Fourier coefficients δ_s^k from the terms $\mathcal{D}_s^j$.

If the initial density operator and observable operator fulfill certain conditions (excitation–detection symmetry), it is possible to derive the coefficients $\mathcal{D}_s^j$ from $\mathcal{E}_s^j$ directly, saving much calculation time (*22*).

The NMR signal at time point $t = j\tau$ is given by

$$s(j\tau) = (Q_{\mathrm{obs}}|\hat{A}_j|\rho(0)). \qquad [112]$$

By inserting a unity superoperator, this may be expressed as

$$s(j\tau) = \sum_s (Q_{\mathrm{obs}}|\hat{A}_j|Q_s^R)(Q_s^L|\rho(0))$$

$$= \sum_s \mathcal{D}_s^j\mathcal{E}_s^0\exp\{z_s j\tau\}. \qquad [113]$$

By employing the Fourier expansion of $\mathcal{D}_s^j$, we get

$$s(j\tau) = \sum_s \sum_k a_s^k\exp\{(i\omega_s^k - \lambda_s)j\tau\} \qquad [114]$$

where

$$a_s^k = \delta_s^k\mathcal{E}_s^0$$

$$\omega_s^k = \mathrm{Im}\{z_s\} + \frac{2\pi k}{T}$$

$$\lambda_s = -\mathrm{Re}\{z_s\}. \qquad [115]$$

This equation shows that each effective Liouvillian eigenvalue z_s contributes a manifold of sidebands to the spectrum, spaced in frequency by the inverse of the modulation period $2\pi/T$. The complex amplitude of each sideband is given by a_s^k. The center frequency of the manifold ω_s^0 is the imaginary part of the eigenvalue z_s. All peaks in the same manifold have the same peak width, specified by λ_s, which is given by minus the real part of z_s. All of these parameters are readily calculated numerically.

For a powder average simulation, the spectrum must be summed over a large number of molecular orientations Ω_{MR}.

As shown below, the angle γ_{MR} may be handled separately, but this still leaves the integration over α_{MR} and β_{MR}. In practice, this is done by dividing the complex plane into a two-dimensional grid of desired resolution, with one axis representing the peak halfwidths λ_s, and the other axis representing the peak frequencies ω_s^k. For each molecular orientation, the amplitudes a_s^k, frequencies ω_s^k, and peak halfwidths λ_s are evaluated for all eigenvalue indices s and sideband indices k. Each complex amplitudes a_s^k is added to the grid point which is nearest to the (frequency, peak width) coordinate (ω_s^k, λ_s). The complete amplitude matrix is built up by repeating the calculation for all eigenvalue and sideband indices and all molecular orientations.

Each slice through the matrix of complex amplitudes, taken parallel to the frequency axis, represents a set of peaks with different frequencies but identical widths. Each of these slices is converted into a subspectrum by (i) inverse Fourier transformation, (ii) multiplication by an exponential decay function with a decay rate appropriate to the peak width parameter λ for that slice, and (iii) forward Fourier transformation. Repetition of the calculation for all slices and summation of the subspectra yields the total powder average spectrum. The conversion of the two-dimensional amplitude matrix into a spectrum is only performed when the entire powder average is complete. If many orientations are involved, this step does not represent a large fraction of the total computational time.

We now turn to the special treatment of the Euler angle γ_{MR}. Several groups have shown that the average over the Euler angle γ_{MR} may be handled implicitly in the Hilbert space COMPUTE algorithm (21–23). The reduction of the powder average to a two-angle integration leads to an increase in computation speed by a factor of at least 5 in most cases. We show below that L-COMPUTE allows a similar acceleration.

If RF fields are absent, a change in the Euler angle γ_{MR} is equivalent to a cyclic permutation of the periodic Liouvillian. The average over γ_{MR} is therefore a *carousel average* over all cyclic permutations of the periodic perturbation (22, 53). In the discussion below, γ_{MR} averaging is expressed in terms of an average over the cyclic permutation index p.

Suppose that p elements $\hat{L}_1 \ldots \hat{L}_p$ are moved from the front to the back of the periodic sequence of Liouvillians. This cyclically permuted sequence is denoted by $[p]$ in the following discussion. The accumulated propagators for the permuted and nonpermuted sequences are related through

$$\hat{A}_j^{[p]} = \hat{A}_{p+j}^{[0]}\{\hat{A}_p^{[0]}\}^{-1}$$

$$\hat{A}_n^{[p]} = \hat{A}_p^{[0]}\hat{A}_n^{[0]}\{\hat{A}_p^{[0]}\}^{-1}. \qquad [116]$$

The cyclic permutation does not change the eigenvalues ν_s of the period propagator. The right eigenkets and left eigenbras, on the other hand, are modified by the cyclic permutation, according to

$$|Q_s^R[p]) = \hat{A}_p^{[0]}|Q_s^R[0])$$

$$(Q_s^L[p]| = (Q_s^L[0]|\{\hat{A}_p^{[0]}\}^{-1}. \qquad [117]$$

The excitation and detection factors for the cyclically permuted sequence are therefore

$$\mathscr{E}_s^j[p] = (Q_s^L[p]|\{\hat{A}_j^{[p]}\}^{-1}|\rho(0))\exp\{+z_s j\tau\}$$

$$= \mathscr{E}_s^{p+j}[0]\exp\{-z_s p\tau\} \qquad [118]$$

and

$$\mathscr{D}_s^j[p] = (Q_{\text{obs}}|\{\hat{A}_j^{[p]}|Q_s^R[p])\exp\{-z_s j\tau\}$$

$$= \mathscr{D}_s^{p+j}[0]\exp\{-z_s p\tau\} \qquad [119]$$

The NMR signal for the cyclically permuted sequence at time $t = j\tau$ may therefore be written

$$s^{[p]}(j\tau) = \sum_s \mathscr{D}_s^j[p]\mathscr{E}_s^0[p]\exp\{z_s j\tau\}$$

$$= \sum_s \mathscr{D}_s^{p+j}[0]\mathscr{E}_s^p[0]\exp\{z_s j\tau\}. \qquad [120]$$

By using the Fourier series expansions of the excitation and detection factors, one obtains the NMR signal for the cyclically permuted sequence,

$$s^{[p]}(j\tau) = \sum_s \sum_k a_s^k[p]\exp\{(i\omega_s^k - \lambda_s)j\tau\}, \qquad [121]$$

with the sideband amplitudes

$$a_s^k[p] = \sum_{k'} \delta_s^k[0]\epsilon_s^{k'}[0]\exp\{i2\pi(k + k')p/n\}. \qquad [122]$$

Note that the sideband frequencies ω_s^k and peak widths λ_s are unaffected by the cyclic permutation.

The NMR signal may be averaged implicitly over all cyclic permutations p. Denoting this carousel average by angled brackets, the NMR signal is

$$\langle s(j\tau) \rangle = \sum_s \sum_k \langle a_s^k \rangle\exp\{(i\omega_s^k - \lambda_s)j\tau\}, \qquad [123]$$

where

$$\langle a_s^k \rangle = n^{-1}\sum_{p=1}^n a_s^k[p] \cong \delta_s^k[0]\epsilon_s^{-k}[0]. \qquad [124]$$

The last line is exact if n is sufficiently large. This equation implies that the γ_{MR}-averaged sideband amplitudes are obtained by combining the excitation and detection sideband amplitudes ϵ_s^k and δ_s^k in complementary pairs. An explicit integration over γ_{MR} is unneccessary. This is a generalization of the Hilbert space result (21–23).

To calculate the full powder average, the calculation is repeated for a set of α_{MR} and β_{MR} values. The resulting two-dimensional matrix of complex amplitudes is handled as described before.

The result in Eq. [124] does not rely on a particular relationship of the initial density operator and the observable operator. However, application of this result is restricted to problems in which a change in γ_{MR} is equivalent to a cyclic permutation of the spin system Liouvillian. This is correct if resonant radiofrequency fields are absent or in the presence of a time-independent RF field. Apart from RR calculations, this result should be useful for calculating powder MAS spectra in the presence of chemical exchange (47, 79). The effect of unresolved homonuclear couplings could also be modeled by Liouville space calculations including irreversible damping of the transverse coherences.

To summarize, the L-COMPUTE algorithm, incorporating implicit averaging over the angle γ_{MR}, involves the following steps:

1. Initialize the matrix of complex amplitudes, and the frequency domain spectrum, to zero.

2. Select a pair of molecular orientational angles α_{MR} and β_{MR}.

3. If the Liouvillian is block-diagonal, handle the blocks separately. Steps 4–13 below refer to each individual block.

4. Set up the series of Liouvillians $\hat{L}_j$ at n time points within one rotor period. In the case of spin-pair RR calculations, this corresponds to evaluating Eq. [36] or Eq. [37] for a set of evenly spaced time points within one rotor period. For maximum computational efficiency, n should be an integer power of 2.

5. Diagonalize each Liouvillian $\hat{L}_j$, and estimate the set of propagators $\hat{S}_j$ through Eq. [99].

6. Multiply the propagators $\hat{S}_j$ together to obtain the accumulated propagators $\hat{A}_j$, including the period propagator $\hat{A}_n$ (Eq. [101]).

7. Diagonalize the period propagator $\hat{A}_n$ to obtain the eigenvalues v_s and right eigenkets $|Q_s^R\rangle$. Form a matrix $\hat{X}$ with columns given by the right eigenkets. Take the inverse of this matrix to obtain $\hat{X}^{-1}$. The left eigenbras $\langle Q_s^L|$ are given by the rows of $\hat{X}^{-1}$.

8. Take the logarithm of the complex numbers v_s and divide by the period T to obtain the effective Liouvillian eigenvalues z_s (Eq. [107]).

9. For each eigenvalue z_s, use the eigenkets and eigenbras to calculate the set of excitation coefficients $\mathscr{E}_s^j$, with $j = 1 \ldots n$ (Eq. [109]).

10. Perform a fast Fourier transform on the sets of numbers $\mathscr{E}_s^j$ to obtain the Fourier coefficients ϵ_s^k.

11. In the case of excitation–detection symmetry (see Ref. (22)), derive the detection coefficients δ_s^k from the excitation coefficients ϵ_s^k. In the general case, calculate the set of detection coefficients $\mathscr{D}_s^j$ separately using Eq. [109] and perform a second fast Fourier transform to obtain δ_s^k.

12. Calculate the set of γ_{MR}-averaged complex amplitudes $\langle a_s^k \rangle$ by multiplying the numbers δ_s^k and ϵ_s^{-k} according to Eq. [124].

13. Add the complex amplitude $\langle a_s^k \rangle$ to the two-dimensional amplitude matrix, at the coordinates defined by the frequency ω_s^k and peak width λ_s, as given in Eq. [115]. Repeat for each sideband index k and each eigenvalue index s.

14. Repeat steps 4–13 for the other blocks of the Liouvillian.

15. Repeat steps 2–14 for all pairs of Euler angles $\{\alpha_{MR}, \beta_{MR}\}$.

16. Convert the two-dimensional amplitude matrix into a spectrum. First initialize the spectrum to zero. Then perform an inverse Fourier transformation on each row of the matrix, multiply by an exponential decay function, perform a forward Fourier transformation, and add to the spectrum. For each row, the rate constant for the exponential decay is different and is given by the peak width coordinate λ. Add together the spectra generated by all rows.

Code for L-COMPUTE simulations of RR spectra may be downloaded from the internet site www.fos.su.se/~mhl.

ACKNOWLEDGMENTS

REFERENCES

1. E. R. Andrew, A. Bradbury, R. G. Eades, and V. T. Wynn, *Phys. Lett.* **4,** 99 (1963).

2. E. R. Andrew, S. Clough, L. F. Farnell, T. D. Gledhill, and I. Roberts, *Phys. Lett.* **21,** 505 (1966).

3. M. G. Colombo, B. H. Meier, and R. R. Ernst, *Chem. Phys. Lett.* **146,** 189 (1988).

4. D. P. Raleigh, M. H. Levitt, and R. G. Griffin, *Chem. Phys. Lett.* **146,** 71 (1988).

5. M. H. Levitt, D. P. Raleigh, F. Creuzet, and R. G. Griffin, *J. Chem. Phys.* **92,** 6347 (1990).

6. T. Karlsson, M. Helmle, N. D. Kurur, and M. H. Levitt, *Chem. Phys. Lett.* **247,** 534 (1995).

7. T. Karlsson and M. H. Levitt, *J. Chem. Phys.* **109,** 5493 (1998).

8. X. Feng, P. J. E. Verdegem, Y. K. Lee, M. Helmle, S. C. Shekar, J. Lugtenburg, H. J. M. de Groot, and M. H. Levitt, *Solid State NMR* **14,** 81 (1999).

9. P. R. Costa, B. Sun, and R. G. Griffin, *J. Am. Chem. Soc.* **119,** 10821 (1997).

10. F. Creuzet, A. McDermott, R. Gebhardt, K. van der Hoef, M. B. Spijker-Assink, J. Herzfeld, J. Lugtenburg, M. H. Levitt, R. G. Griffin, *Science* **251,** 783 (1991).

11. O. B. Peersen, S. Yoshimura, H. Hojo, S. Aimoto, and S. O. Smith, *J. Am. Chem. Soc.* **114,** 4332 (1992).

12. S. O. Smith, *Curr. Opin. Struct. Biol.* **3,** 755 (1993).

13. P. J. E. Verdegem, M. Helmle, J. Lugtenburg, and H. J. M. de Groot, *J. Am. Chem. Soc.* **119,** 169 (1997).

14. D. A. Middleton, R. Robins, X. Feng, M. H. Levitt, I. D. Spiers, C. H. Schwalbe, D. G. Reid, and A. Watts, *FEBS Lett.* **410,** 269 (1997).

15. P. T. Lansbury, P. R. Costa, J. M. Griffiths, E. J. Simon, M. Auger, K. J. Halverson, D. A. Kocisko, Z. S. Hendsch, T. T. Ashburn, R. G. S. Spencer, P. Tidor, and R. G. Griffin, *Nature Struct. Biol.* **2,** 990 (1995).

16. P. R. Costa, D. A. Kocisko, B. Q. Sun, P. T. Lansbury, and R. G. Griffin, *J. Am. Chem. Soc.* **119,** 10487–10493 (1997).

17. J. Heller, A. C. Kolbert, R. Larsen, M. Ernst, T. Bekker, M. Baldwin, S. B. Prusiner, A. Pines, and D. Wemmer, *Protein Sci.* **5,** 1655 (1996).

18. E. R. Andrew, A. Bradbury, and R. G. Eades, *Nature* **183,** 1802 (1959).

19. I. J. Lowe, *Phys. Rev. Lett.* **2,** 285 (1959).

20. M. Edén, Y. K. Lee, and M. H. Levitt, *J. Magn. Reson. A* **120,** 56 (1996).

21. T. Charpentier, C. Fermon, and J. Virlet, *J. Magn. Reson.* **132,** 181 (1998).

22. M. H. Levitt and M. Edén, *Mol. Phys.* **95,** 879 (1998).

23. M. Hohwy, H. Bildsøe, H. J. Jakobsen, and N. C. Nielsen, *J. Magn. Reson.* **136,** 6 (1999).

24. W. P. Rothwell and J. S. Waugh, *J. Chem. Phys.* **74,** 2721 (1981).

25. D. L. VanderHart, W. L. Earl, and A. N. Garroway, *J. Magn. Reson.* **44,** 361 (1981).

26. P. Tekely, P. Palmas, and D. Canet, *J. Magn. Reson. A* **107,** 129 (1994).

27. D. L. VanderHart and G. C. Campbell, *J. Magn. Reson.* **134,** 88 (1998).

28. M. Edén and M. H. Levitt, *J. Chem. Phys.,* in press.

29. T. G. Oas, R. G. Griffin, and M. H. Levitt, *J. Chem. Phys.* **89,** 692 (1988).

30. M. H. Levitt, T. G. Oas, and R. G. Griffin, *Isr. J. Chem.* **28,** 271 (1988).

31. A. E. Bennett, C. M. Rienstra, M. Auger, K. V. Lakshmi, and R. G. Griffin, *J. Chem. Phys.* **103,** 1 (1995).

32. J. R. Sachleben, S. Caldarelli, and L. Emsley, *J. Chem. Phys.* **104,** 2518 (1996).

33. T. Hamanaka, T. Mitsui, T. Ashida, and M. Kakudo, *Acta Cryst.* **B28,** 214 (1972).

34. M. Groesbeek and J. Lugtenburg, *Photochem. Photobiol.* **56,** 903–908 (1992).

35. M. H. Levitt, *J. Magn. Reson.* **126,** 164 (1997).

36. D. A. Varshalovich, A. N. Moskalev, and V. K. Kheronskii, "Quantum Theory of Angular Momentum," World Scientific, Singapore (1988).

37. J. Jeener, *Adv. Magn. Reson.* **10,** 1 (1982).

38. M. H. Levitt and L. Di Bari, *Phys. Rev. Lett.* **69,** 3124 (1992).

39. M. H. Levitt and L. Di Bari, *Bull. Magn. Reson.* **16,** 92 (1994).

40. A. G. Redfield, *Adv. Magn. Reson.* **1,** 1 (1965).

41. R. R. Ernst, G. Bodenhausen, and A. Wokaun, "Principles of Nuclear Magnetic Resonance in One and Two Dimensions," Clarendon Press, Oxford (1987).

42. G. Bodenhausen, H. Kogler, and R. R. Ernst, *J. Magn. Reson.* **58,** 370 (1984).

43. M. Goldman, *J. Magn. Reson.* **60,** 437 (1984).

44. Y. Zur, M. H. Levitt, and S. Vega, *J. Chem. Phys.* **78,** 5293 (1983).

45. A. Schmidt, S. O. Smith, D. P. Raleigh, J. E. Roberts, R. G. Griffin, and S. Vega, *J. Chem. Phys.* **88,** 4284 (1986).

46. T. Nakai and C. A. McDowell, *J. Chem. Phys.* **96,** 3452 (1992).

47. A. Schmidt, S. O. Smith, D. P. Raleigh, J. E. Roberts, R. G. Griffin, and S. Vega, *J. Chem. Phys.* **88,** 4284 (1986).

48. G. J. Boender, S. Vega, and H. J. M. de Groot, *Mol. Phys.* **95,** 921–934 (1998).

49. U. Haeberlen and J. S. Waugh, *Phys. Rev.* **175,** 453 (1968).

50. U. Haeberlen, "High Resolution NMR in Solids. Selective Averaging," Academic Press, New York (1976).

51. The Magnus expansion terms are indexed according to their order in a perturbation expansion. The older literature on average Hamiltonian theory employs indices which are one less than those given here.

52. O. N. Antzutkin, personal communication.

53. M. H. Levitt, *J. Magn. Reson.* **82,** 427 (1989).

54. A. Pines, M. G. Gibby, and J. S. Waugh, *J. Chem. Phys.* **59,** 569 (1973).

55. H. M. McConnell, *J. Chem. Phys.* **28,** 430 (1958).

56. S. Alexander, *J. Chem. Phys.* **37,** 967 (1962).

57. S. Alexander, *J. Chem. Phys.* **37,** 974 (1962).

58. R. M. Lynden-Bell, *Prog. NMR Spectrosc.* **2,** 163 (1967).

59. F. A. L. Anet and D. J. O'Leary, *J. Magn. Reson.* **86,** 358 (1990).

60. C. S. Johnson and J. C. Tully, *J. Chem. Phys.* **40,** 1744 (1964).

61. A. Abragam, "The Principles of Nuclear Magnetism," Clarendon Press, Oxford (1961).

62. G. Sinning, M. Mehring, and A. Pines, *Chem. Phys. Lett.* **43,** 382 (1976).

63. M. Mehring and G. Sinning, *Phys. Rev.* **15,** 2519 (1977).

64. M. Mehring, "High Resolution NMR in Solids," 2nd. ed., Springer, Berlin (1982).

65. H. W. Spiess, U. Haeberlen, and H. Zimmerman, *J. Magn. Reson.* **25,** 55 (1977).

66. Z.-H. Gan, J. C. Facelli, and D. M. Grant, *J. Chem. Phys.* **89,** 5542 (1988).

67. M. Ernst, A. Verhoeven, and B. H. Meier, *J. Magn. Reson.* **130,** 176 (1998).

68. G. S. Harbison, *J. Am. Chem. Soc.* **115,** 3026 (1993).

69. The parameters used in the simulations of 11,20-^{13}C$_2$-all-*E*-retinal are as follows: ^{13}C Larmor frequency $\omega_0/2\pi = -100.65$ MHz; Chemical shift anisotropy of C11 site $\delta_k^{aniso} = -112.8$ ppm; CSA asymmetry parameter for C11 site $\eta_k = 0.72$; Euler angles relating CSA of C11 site to molecular axis frame, with *z*-axis along C11–C12 vector: $\{\alpha_{PM}^k, \beta_{PM}^k, \gamma_{PM}^k\} = \{-31.6°, 86.0°, -87.5°\}$. Chemical shift anisotropy of C20 site $\delta_j^{aniso} = -15.6$ ppm; CSA asymmetry parameter for C20 site $\eta_j = 1.00$; Euler angles relating CSA of C20 site to molecular axis frame: $\{\alpha_{PM}^j, \beta_{PM}^j, \gamma_{PM}^j\} = \{-0.3°, 57.2°, -0.3°\}$; Isotropic chemical shift difference $\delta_j^{iso} - \delta_k^{iso} = -121.7$

ppm; Through-space dipole–dipole coupling $b_{jk}/2\pi = -293$ Hz; J-coupling $J_{jk} = 3.0$ Hz.

70. K. Schmidt-Rohr and H. W. Spiess, "Multidimensional Solid-State NMR and Polymers," Academic Press, London (1994).

71. M. Ernst, S. Bush, A. C. Kolbert, and A. Pines, *J. Chem. Phys.* **105,** 3387 (1996).

72. J. Heller, R. Larsen, M. Ernst, A. C. Kolbert, M. Baldwin, S. B. Prusiner, D. E. Wemmer, and A. Pines, *Chem. Phys. Lett.* **251,** 223 (1996).

73. E. Kundla and E. Lippmaa, *J. Chem. Phys.* **102,** 1569 (1995).

74. D. L. Vanderhart, *J. Chem. Phys.* **84,** 1196 (1986).

75. M. P. Augustine, K. W. Zilm, and D. B. Zax, *J. Chem. Phys.* **98,** 9432 (1993).

76. D. B. Zax, *J. Chem. Phys.* **105,** 6616 (1996).

77. The parameters used in the simulations of $[^{13}C_2, {}^{15}N]$-glycine are as follows: ^{13}C Larmor frequency $\omega_0/2\pi = -50.345$ MHz; Chemical shift anisotropy of C1 site $\delta_k^{aniso} = -74.5$ ppm; CSA asymmetry parameter for C1 site $\eta_k = 0.884$; Euler angles relating CSA of C1 site to molecular axis frame, with z-axis along C1–C2 vector: $\{\alpha_{PM}^k, \beta_{PM}^k, \gamma_{PM}^k\} = \{-0.7°, 88.5°, 42.5°\}$. Chemical shift anisotropy of C2 site $\delta_j^{aniso} = -19.4$ ppm; CSA asymmetry parameter for C2 site $\eta_j = 0.983$; Euler angles relating CSA of C2 site to molecular axis frame: $\{\alpha_{PM}^j, \beta_{PM}^j, \gamma_{PM}^j\} = \{-99.4°, 146.0°, 139.0°\}$; Isotropic chemical shift difference $\delta_j^{iso} - \delta_k^{iso} = -130.94$ ppm; Through-space dipole–dipole coupling $b_{jk}/2\pi = -2135$ Hz; J-coupling $J_{jk} = 53.0$ Hz. These parameters are adapted from the data given in Ref. (*80*) and concern only one of the two molecules in the crystallographic unit cell. The ^{15}N spin is ignored.

78. T. Karlsson, M. Edén, P. J. E. Verdegem, J. Lugtenburg, and M. H. Levitt, to be published.

79. M. J. Duer and M. H. Levitt, *Sol. State Nucl. Magn. Reson.* **1,** 211 (1992).

80. R. A. Haberkorn, R. E. Stark, H. van Willigen, and R. G. Griffin, *J. Am. Chem. Soc.* **103,** 2534 (1981).